Tuning of Cr–Cr magnetic exchange through chalcogenide linkers in Cr_2 molecular dimers

Eranga H. Gamage,[a,b] Raquel A. Ribeiro,[b,c] Colin P. Harmer,[a,b] Paul C. Canfield,[b,c] Andrew Ozarowski,[d,*] Kirill Kovnir[a,b,*]

[a] *Department of Chemistry, Iowa State University, Ames, Iowa 50011, USA*

[b] *Ames Laboratory, U.S. Department of Energy, Ames, Iowa 50011, USA*

[c] *Department of Physics and Astronomy, Iowa State University, Ames, Iowa, 50011, USA*

[d] *National High Magnetic Field Laboratory, 1800 E Paul Dirac Dr, Tallahassee, FL 32310, USA*

Abstract

A set of three Cr-dimer compounds, $Cr_2Q_2(en)_4X_2$ (*Q*: S, Se; *X*: Br, Cl; *en*: ethylenediamine), with monoatomic chalcogenide bridges has been synthesized via a single–step solvothermal route. Chalcogenide linkers mediate magnetic exchange between Cr^{3+} centers while bidentate ethylenediamine ligands complete the distorted octahedral coordination of Cr centers. Unlike the compounds previously reported, none of the chalcogenide atoms are connected to extra ligands. Magnetic susceptibility studies indicate antiferromagnetic coupling between Cr^{3+} centers, which are moderate in $Cr_2Se_2(en)_4X_2$ and stronger in $Cr_2S_2(en)_4Cl_2$. Fitting the magnetic data require a biquadratic exchange term. High frequency EPR spectra showing characteristic signals due to coupled $S = 1$ spin states, could be interpreted in terms of the "giant spin" Hamiltonian. A fourth compound, $Cr_2Se_8(en)_4$, has a single diatomic Se bridge connecting the two Cr^{3+} centers and shows weak ferromagnetic exchange interactions. This work demonstrates the tunability in strength and type of exchange interactions between metal centers by manipulating the interatomic distances and number of bridging chalcogenide linkers.

Introduction

Since the successful studies of copper acetate monohydrate by electronic paramagnetic resonance (EPR),[1,2] accompanied by important theoretical work,[3] extensive research has been performed on a wide variety of binuclear or polynuclear complexes with various mono– or polyatomic bridges.[4–8] A theoretical analysis demonstrated that the bridging species significantly influence the Jahn–Teller distortion associated with the metal centers.[9] A computational study based on an extended Hückel type calculations conducted by *Hoffman et al*. showed that the metal–metal interactions in bridged dimer complexes are facilitated by coupling through the orbitals of the bridging groups.[10] As a result of these findings, scientists gained insight into the role of many biologically important *d*–block metal dimeric compounds with respect to metabolism, catalysis, and drug delivery. Many oxo–bridged transition metal dimers have been theoretically studied as molecular magnetic materials to elucidate their nearest neighbor interactions.[11] Ruthenium dimers are extensively studied for their ability to catalyze water oxidation[12,13] and as promising pharmaceutical candidates.[14,15] Binuclear cobalt complexes have been shown as promising agents for electrocatalytic proton reduction[16] and slow magnetic relaxation.[17,18] *Gennari and Duboc et al.* discovered a non–Heme manganese dimer capable of effectively reacting with oxygen[19] while exchange and magnetic anisotropy effects were studied in several different manganese dimers.[20,21] A vast majority of dimer related research is focused on copper dimers for their susceptibility to be bridged by diverse bulky organic ligands resulting in a variety of magnetic and super-exchange interactions.[22–26]

Complexes where transition metal atoms are bridged by heavier elements with stronger spin-orbit coupling are relatively rare and have not been intensively investigated. *Lledos et al.* reported an *ab initio* study on Pt_2S_2 rings to understand the factors that govern the structural preferences.[27] Magnetic susceptibility and Mössbauer experiments demonstrated the presence of mixed–valent $[Fe_2S_2]^+$ dimers in iron–sulfur clusters in ferredoxins and other biological systems.[28–30] Binuclear complexes of many–electron metals like Cr are much more challenging to characterize, particularly from the viewpoint of EPR as a large zero–field splitting is often observed, making the standard *X*- or even *Q*-Band EPR inaccessible.[31–33] Despite this, extensive magnetic and EPR studies have been conducted on different kinds of Cr^{III}–Cr^{III} dimers bridged by a variety organic moieties following both experimental[34–39] and theoretical approaches.[40–44] *Semenaka et al.* investigated the Cr–Cr interactions in the weakly exchange–coupled alkoxo–bridged heterometallic Zn_2Cr_2 complexes by means of magnetometry, high frequency EPR spectroscopy, and density functional theory (DFT) calculations.[45]

The possibility of utilizing selenium bridged transition metal dimer complexes as catalysts for organic reactions has been studied over the past few decades.[46–50] Chemistry of the linear Cr_2Se and butterfly Cr_2Se_2 complexes have been explored by different synthetic and characterization approaches.[51–53] In this work we report the synthesis, crystal structure, and properties of three new molecular compounds $Cr_2Q_2(en)_4X_2$ (*Q*: S, Se; *X*: Br, Cl; *en*: ethylenediamine), all with a Cr_2Q_2 rhombus core. An important feature of these compounds is that the bridging selenium atoms are not connected to any other organic ligands. Magnetic studies coupled with high–frequency EPR reveal antiferromagnetic interactions between Cr centers in $Cr_2Q_2(en)_4X_2$. A reaction of

$Cr_2Se_2(en)_4Br_2$ with excess Se resulted in the formation of another Cr_2 compound with a diatomic selenium bridge, $Cr_2Se_8(en)_4$, previously reported by *Dehnen et al.*[54] Magnetic susceptibility studies show that replacement of monoatomic Se bridge with the diatomic one leads to the change of the type of Cr–Cr interactions from antiferromagnetic to ferromagnetic.

Experimental Section

Warning: Reactions conducted with Se using amine solvents can give out toxic fumes. Opening of the reaction autoclaves should only be done in well ventilated areas, like a fumehood. Splashing of the solvent may occur upon opening the autoclaves. Wearing of proper protective equipment including face-shields, long-sleeve gloves, and tight-cuff lab coats and placing the furnaces in well-ventilated spaces such as fume hoods is highly recommended. Filtration of the samples and further sample handling should be conducted in a fumehood with emergency exhaust activated due to the strong odor.

Synthesis of $Cr_2Se_2(en)_4X_2$ (X = Br, Cl)

$Cr_2Se_2(en)_4Br_2$ was synthesized by the reaction of 1 mmol of chromium powder (–100+325 mesh, Alfa Aesar, 99.97%) and 1 mmol of selenium powder (Sigma Aldrich, >99.5%) with 100 mg of ammonium bromide (Alfa Aesar, 99%) in 10 mL of ethylenediamine (*en*) (Alfa Aesar, 99%) under solvothermal conditions for 3–5 days at 200 °C. After which time, the autoclave vessel was cooled naturally to room temperature in the fumehood. The product was then filtered with aliquots of absolute ethanol and appeared as black shiny needles with silver chunks (Fig. S1). The silvery chunks were identified to be recrystallized chromium as indicated by the peak at $2\theta = 44.4°$ attributed to elemental chromium in the powder X–ray diffraction (PXRD) pattern. The $Cr_2Se_2(en)_4Br_2$ crystals looked dull green in color when finely ground. The chloride analogue, $Cr_2Se_2(en)_4Cl_2$ was formed under similar conditions when ammonium bromide was replaced with ammonium chloride (Fisher Scientific, 99%).

$Cr_2Se_2(en)_4Br_2$ and $Cr_2Se_2(en)_4Cl_2$ were also synthesized when Cr metal was replaced with chromium (III) bromide hexahydrate (Strem Chemicals, Incorporated, 99%) and chromium (III) chloride hexahydrate (Alfa Aesar, 98%), respectively, in the presence of respective NH_4X (Table S1). Using hydrous Cr halides, experiments were conducted to optimize the reaction conditions that would result in no residual elemental Cr in the final product. During the optimization process, the samples were visually examined under the optical microscope to check for recrystallized chunks of elemental Cr and the appearance of the Cr peak in the PXRD pattern was monitored. The final optimized reaction conditions: solvothermal reaction of 1 mmol of the hydrous Cr halide, 1.33 mmol of Se and 150 mg of the corresponding NH_4X in 10 mL of *en* for 3–5 days at 200 °C. Such reactions provided samples with no detected Cr impurity and were used for property measurements. All the reactions were carried out under normal atmospheric conditions and the resulting samples could be stored in vials on the benchtop for several months with no signs of decomposition or oxidation.

Synthesis of $Cr_2S_2(en)_4Cl_2$

The sulfur analogue, $Cr_2S_2(en)_4Cl_2$, was synthesized by a reaction of chromium (III) chloride hexahydrate and sulfur powder (–100 mesh, Alfa Aesar, 99.5%) in a 1:1 molar ratio with 100 mg of ammonium chloride added to *en* solution (Table S1). Reactions were prepared and processed under the conditions mentioned above, yielding a dark shiny green-black powder which gave an experimental PXRD pattern resembling its calculated pattern. For synthesis of $Cr_2S_2(en)_4Cl_2$, thiourea (Sigma Aldrich, 99%) can also be used as the source of sulfur in a 1:2 molar ratio. In turn, reactions of metallic chromium powder with sulfur powder failed to yield the dimer phase and resulted in recrystallized chromium as the only solid product. Due to the inability to grow single crystals of $Cr_2S_2(en)_4Cl_2$, the crystal structure was established by high resolution synchrotron powder X–ray diffraction. All attempts to synthesize the bromide analogue of $Cr_2S_2(en)_4Cl_2$ were unsuccessful.

Synthesis of $Cr_2Se_8(en)_4$

Treatment of $Cr_2Se_2(en)_4Br_2$ phase with selenium (1:8 molar ratio) in an of excess *en* under similar solvothermal conditions at 200 °C led to the formation of the $Cr_2Se_8(en)_4$ phase (Table S1). The reaction vessel was cooled naturally to room temperature and the products were filtered with absolute ethanol. $Cr_2Se_8(en)_4$ crystallizes as shiny black crystals (~1 mm^3) forming clusters clearly visible to the naked eye (Fig. S2). The sample was dried on a petri dish under normal atmospheric conditions after which the crystals were handpicked and finely ground for property measurements.

Characterization

All $Cr_2Q_2(en)_4X_2$ (Q = S, Se; X = Br, Cl) and $Cr_2Se_8(en)_4$ samples were synthesized outside the glovebox due to their air and moisture stability. After filtration, the samples were stored in vials and kept on a benchtop under ambient conditions. PXRD experiments were conducted on a bench top Rigaku 600 Miniflex with a Cu-K_α radiation (λ = 1.54185 Å) and a Ni-K_β filter. Fluorescence of Cr atoms in the sample upon exposure to incident Cu–K_α radiation, grease used to stick powder to the plate, or the presence of trace amorphous impurities contribute to background in the PXRD patterns.

In-situ PXRD experiments were conducted on beamline 17–BM–B (λ = 0.24153 Å) at the Advanced Photon Source (APS) in Argonne National Laboratory (ANL) using the solvothermal setup we reported earlier.[55] High resolution synchrotron PXRD data was obtained through the mail-in program on beamline 11-BM-B (λ = 0.457910 Å) at the APS. A powdered sample of $Cr_2S_2(en)_4Cl_2$ was packed in a 0.8 mm Kapton capillary to conduct a ~1 hour scan in the $0.5° < 2\Theta < 50°$ range at 100 K and Rietveld refinement was performed on the data using GSAS-II software to determine the crystal structure.[56] The initial model derived from the Se analog was used for refinement against the high-resolution synchrotron powder data.

Single crystal diffraction data were collected on a Bruker D8 Venture diffractometer with a Photon100 CMOS detector employing Mo-K_α radiation (λ = 0.71073 Å) at 100 K under a constant flow of dry N_2. Crystal structure refinement was performed using SHELX software package.[57]

Magnetic measurements were performed on a ~40 mg of powdered samples with a Quantum Design SQUID magnetometer MPMS-5. Temperature dependence of magnetization was studied in different applied magnetic fields. Isothermal field–dependence of the magnetization was studied in a 0-7 T field at different temperatures. A non-linear least-squares method was used to fit the magnetic data as described in the Magnetic properties section.

Elemental composition data of the samples were obtained on an Energy Dispersive X-ray Spectrometer FEI Quanta 250 field emission-SEM with EDS detection (Oxford X-Max 80) and Aztec software was used for data analysis. Needles of $Cr_2Se_2(en)_4Br_2$, $Cr_2Se_2(en)_4Cl_2$ and chunks of $Cr_2Se_8(en)_4$ were mounted onto graphite tape for analysis. Normalization of quants obtained at different acquisition sites provided the average composition to be $Cr_{1.9(1)}Se_2Br_{1.9(5)}$, $Cr_{1.9(3)}Se_2Cl_{2.0(4)}$, and $Cr_{1.9(9)}Se_8$ based on normalization to the Se content from crystal structure models. Quants obtained for $Cr_2S_2(en)_4Cl_2$ powder on carbon tape yielded a normalized composition of $Cr_{1.9(1)}S_2Cl_{2.0(1)}$.

The high–field, high–frequency EPR spectra at temperatures ranging from *ca.* 3 K to 290 K were recorded on a home–built spectrometer at the EMR facility of the National High Magnetic Field Laboratory (NHMFL).[58] The instrument is equipped with a superconducting magnet (Oxford Instruments) capable of reaching a field of 17 T. Microwave frequencies over the range 52-630 GHz were generated by a phase-locked Virginia Diodes source, producing a base frequency of 8-18 GHz, which was multiplied by a cascade of frequency multipliers. The instrument is a transmission-type device and uses no resonance cavity. The EPR spectra and magnetic data were simulated using software written by AO, available from the author upon request.

Results and Discussion

Synthesis of $Cr_2Se_2(en)_4X_2$

$Cr_2Se_2(en)_4X_2$ (X = Cl, Br) compounds were first synthesized using elemental chromium as precursor which led to presence of residual chromium metal in the final products. Notable differences in the intensities of peaks between theoretical and experimental PXRD patterns in $Cr_2Se_2(en)_4X_2$ is a result of preferred orientation of the needle–like crystals (Fig. S3). To remove the Cr metal admixture, optimization reactions were carried out by varying the reaction conditions such as elemental ratios and concentrations, reaction duration, temperature, filling fraction of the solvent, and cooling rates (Table S1). But all these attempts failed to deliver a phase pure product with no chromium impurity. However, these optimizations did reveal that $Cr_2Se_2(en)_4X_2$ had a formation window of 180 °C to 230 °C.

A post synthetic recrystallization of $Cr_2Se_2(en)_4Br_2$ was attempted. The compound was not soluble in methanol, ethanol, ethanolamine, dimethylformamide (DMF), dimethyl sulfoxide (DMSO), and diethyl ether. When ethylenediamine was mixed with aqueous potassium hydroxide/glycerol/ethylene glycol, the resulting solvents decomposed the dimer into constituent elements upon heating and stirring. The universal solvent, water, was able to completely dissolve $Cr_2Se_2(en)_4Br_2$. However, in the case of water, the compound did not precipitate out from the cooled filtrate and instead disintegrated into elemental Cr and Se. Since the recrystallization attempts failed, attention was diverted to using different starting materials. When metallic Cr was

replaced by soluble Cr salts under the same conditions, $Cr_2Se_2(en)_4Br_2$ was synthesized as black powder with minimum chromium impurity as evidenced by the PXRD patterns (Fig. 1**)**. Samples synthesized in this manner turned out to be black powders with no residual elemental chromium.

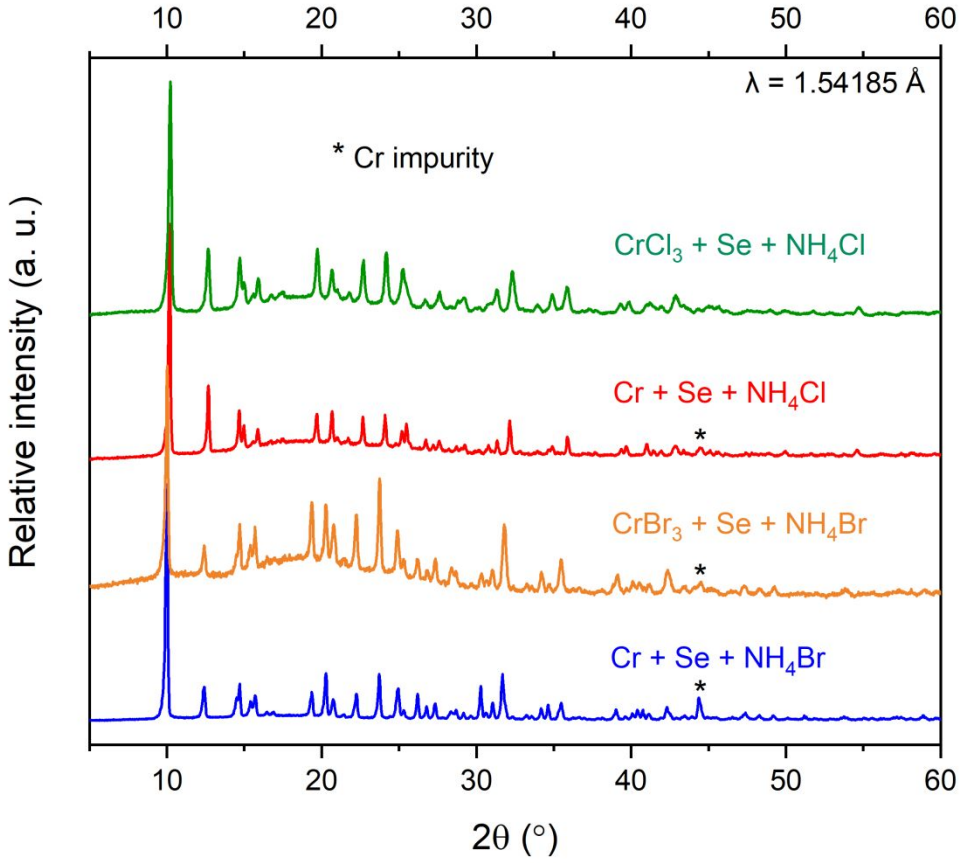

Figure 1. PXRD patterns of $Cr_2Se_2(en)_4X_2$ as synthesized from various reactants.

To gain insight of the mechanism of formation of the $Cr_2Se_2(en)_4Br_2$, *in–situ* powder X-ray diffraction studies were conducted at the 17-BM Advanced Photon Source of Argonne National Laboratory using the solvothermal setup reported elsewhere.[55] Ammonium bromide was dissolved in *en* which was then injected to the silica capillary containing a stoichiometric mixture of chromium and selenium metal powders. This capillary was pressurized with 40 bar argon to mimic solvothermal conditions. Upon heating, selenium peaks diminish fully at its melting point ~220 °C, above which chromium metal was the only crystalline phase detected (Fig. S4). No sign of $Cr_2Se_2(en)_4Br_2$ was observed until 290 °C, where a new peak appeared at 2Θ ~ 1.25° (outlined in orange) which does not match with the most intense first peak of $Cr_2Se_2(en)_4Br_2$ at 2Θ ~ 1.56°. Upon further heating to ~340 °C, or cooling back to room temperature, $Cr_2Se_2(en)_4Br_2$ still did not form. Different concentrations of the reagent and short reaction time used for the *in-situ* experiment are probably the factors which prevent the formation of $Cr_2Se_2(en)_4Br_2$ dimer compound.

Synthesis of $Cr_2S_2(en)_4Cl_2$

The sulfur analogue, $Cr_2S_2(en)_4Cl_2$, can be obtained in a reaction of stoichiometric ratios of $CrCl_3{\cdot}6H_2O$ with sulfur powder or thiourea in an excess of ethylenediamine under similar solvothermal conditions (Table S1). Final products of these reactions were polycrystalline powders with no observed crystals suitable for single crystal X–ray diffraction experiments. The similarities of experimental powder patterns with that of the calculated pattern suggested that the '$Cr_2S_2(en)_4Cl_2$' analogue was formed and was further proved by the shift of peaks to higher angle (Fig. S5). Rietveld refinement was performed on the high–resolution synchrotron PXRD data to obtain the crystal structure of the Cr_2S_2 dimer (Fig. S6). Both sulfur powder and thiourea used as starting materials can yield phase pure $Cr_2S_2(en)_4Cl_2$ under the same solvothermal conditions. Irrespective of the chromium starting material used, replacing ammonium chloride with ammonium bromide failed to produce the sulfur bromide analogue of the dimer. This result suggests that the formation of '$Cr_2S_2(en)_4Br_2$' phase, if exists, is not favored under the mentioned solvothermal conditions.

Synthesis of $Cr_2Se_8(en)_4$

This phase was synthesized when $Cr_2Se_2(en)_4Br_2$ was treated with an excess of selenium in attempts to eliminate leftover chromium metal in the products. A gradual increase in the amount of selenium gives a mixture of $Cr_2Se_2(en)_4Br_2$ and $Cr_2Se_8(en)_4$ until it reaches the stoichiometric ratio giving $Cr_2Se_8(en)_4$ with no admixtures (Table S1). Slight differences in the intensities of peaks in experimental and theoretical PXRD patterns could still be observed (Fig. S7). Shiny black crystal chunks were visible to naked eye and the clusters could be broken up with a needle to isolate the individual crystals. An addition of NH_4Br to this reaction suppresses the formation of $Cr_2Se_8(en)_4$, while favoring the recrystallization of the starting material $Cr_2Se_2(en)_4Br_2$. Post synthetic second treatment of finely ground $Cr_2Se_8(en)_4$ with *en*, leaves the compound unchanged. Contradictory to the report of *Dehnen et al.*,[54] this reaction scheme yields very stable products that do not decompose under normal atmospheric conditions and it was not necessary to use inert conditions for the synthesis. Even though $Cr_2Se_8(en)_4$ is a neutral molecular compound, solubility studies showed it to be insoluble in nonpolar hexane, acetonitrile, and DMF solvents.

Crystal structure of $Cr_2Q_2(en)_4X_2$ (Q = S, Se; X = Cl, Br)

$Cr_2Q_2(en)_4X_2$ compounds crystallize in the monoclinic space group $P2_1/n$ (Table 1). The unit cell volumes of the three isostructural compounds follow the order of $Cr_2S_2(en)_4Cl_2$ < $Cr_2Se_2(en)_4Cl_2$ < $Cr_2Se_2(en)_4Br_2$, in agreement with the ionic radii of constituting elements. The general structure of this dimeric compounds is described using $Cr_2Se_2(en)_4Cl_2$ dimer as a model. The crystal structure of $Cr_2Se_2(en)_4Cl_2$ consists of discrete molecular entities of a Cr dimer connected by two monoatomic selenium bridges, making slightly distorted square Cr_2Se_2 core (Fig. 2A). Crystal structure of a single unit with the atomic displacement parameters (ADPs) is shown in Fig. S8. Cr–Se bond distances vary from 2.460(1) – 2.484(2) Å (Table 2), while ∢ Se–Cr–Se and ∢ Cr–Se–Cr are 88.51(5)° and 91.49(5)° respectively. Cr–Cr bond distance across the core is 3.540(3) Å. Chromium atoms remain six coordinated by bonding to four N atoms from two ethylenediamine ligands. A variation in Cr–N bond distances result in a distorted octahedral geometry (Table 2) and a ~C_{2v} (*mm*2) local symmetry around chromium. Two accompanying Cl^- anions prompt the dimer cation to have a +2 charge, indicating Cr^{3+} and Se^{2-} oxidation states.

Table 1. Single crystal data collection and refinement parameters for $Cr_2Se_2(en)_4Br_2$, $Cr_2Se_2(en)_4Cl_2$ and $Cr_2Se_8(en)_4$. For $Cr_2S_2(en)_4Cl_2$, Rietveld refinement was performed against PXRD data collected at 100 K on beamline 11-BM-B at the APS ANL.

	$Cr_2Se_2(en)_4Br_2$	**$Cr_2Se_2(en)_4Cl_2$**	**$Cr_2S_2(en)_4Cl_2$**	**$Cr_2Se_8(en)_4$**
CSD-number	2144990	2144978	2144988	2144989
specimen type	single crystal	single crystal	powder	single crystal
temperature (K)	100(2)			
source	Mo-K_α	Mo-K_α	synchrotron	Mo-K_α
λ (Å)	0.71073	0.71073	0. 45791	0.71073
space group	$P2_1/n$ (No. 14)			$C2/c$ (No. 15)
a (Å)	6.5052(4)	6.4564(8)	6.2859(7)	27.0369(2)
b (Å)	11.2771(8)	11.1494(2)	11.1758(1)	8.1586(5)
c (Å)	14.1312(1)	13.8458(2)	13.8681(3)	24.1599(2)
β (degrees)	94.494(3)	94.471(3)	94.353(8)	110.438(4)
V (Å^3)	1033.47(1)	993.7(2)	971.42(2)	4993.8(6)
Z	2	2	2	8
form. weight (gmol^{-1})	662.15	573.23	479.43	976.09
ρ_{calc} (g cm^{-3})	2.128	1.916	1.639	2.597
μ (mm^{-1})	8.447	5.033	–	12.545
data/parameters	2383/101	2762/102	28045/78	5771/331
R_1/wR_2	0.033/ 0.058	0.067/0.105	–	0.020/ 0.040
R_{wp}	–	–	0.098	–
GOF	1.04	1.09	1.64	1.07
diff. peak/hole (e·Å^3)	0.88/–0.60	1.15/–1.36	–	1.18/–0.49

Further details of the crystal structure determination may be obtained from Fachinformationszentrum Karlsruhe, Germany, by quoting the CSD depository numbers given in the Table above.

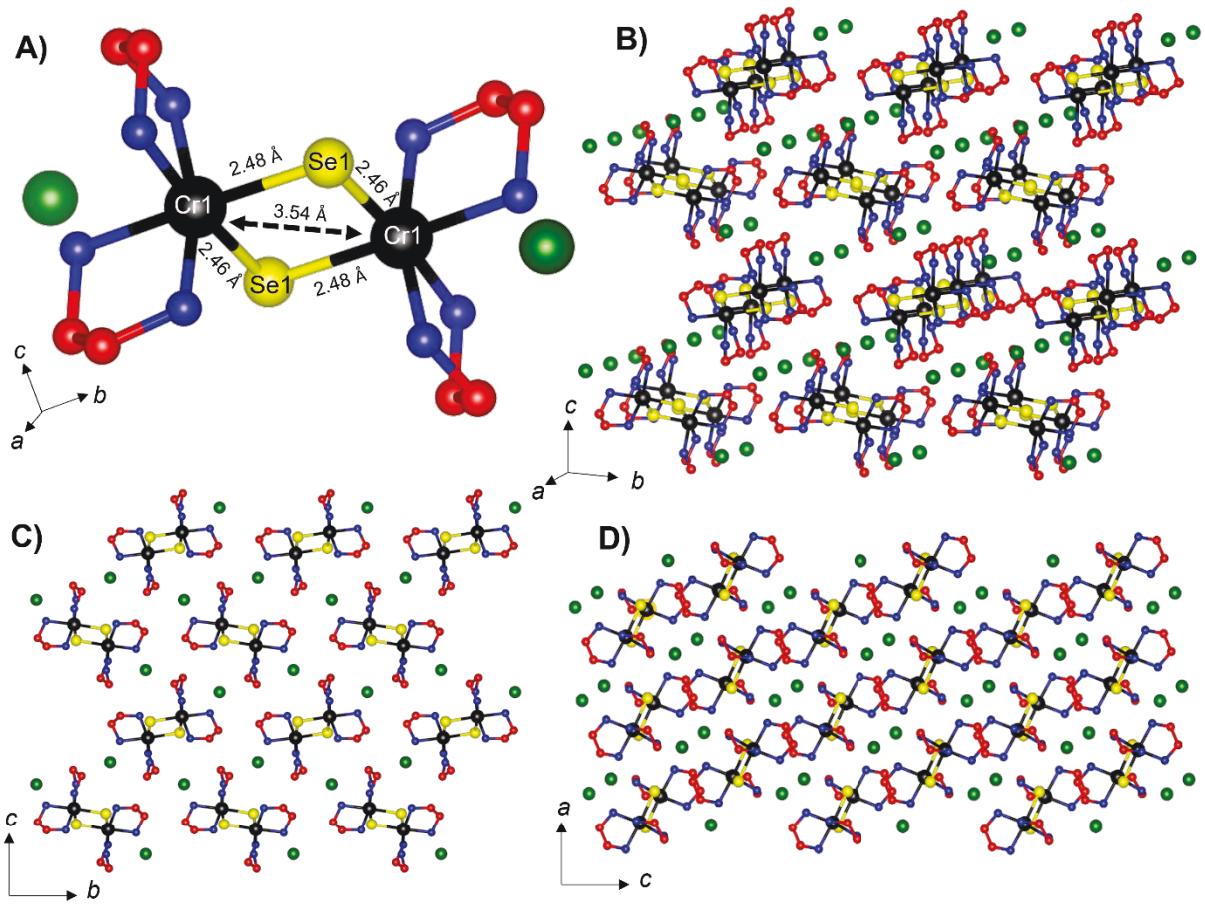

Figure 2. Crystal structure of $Cr_2Se_2(en)_4Cl_2$ dimer phase **A)** Structure of one dimer fragment **B)** General view along [100] direction **C)–D)** View along different crystallographic directions. Cr: black; Se: yellow; N: blue; C: red; Cl: green. All hydrogen atoms are omitted for clarity.

Cr_2Se_2 dimers are stacked along [100] direction and the charge balancing Cl^- ions are arranged in channels along the same direction (Fig. 2B and 2C). Layers of alternating dimer fragments are arranged in ABAB sequence (Fig. 2C). The view along [010] direction shows the Cl^- channels organized in pairs in a diagonal fashion (Fig. 2D). Although the dimers have no covalent connection to each other, the crystal structure is stabilized by van der Waals and electrostatic interactions. 3D packing of the discrete units is supported by N-H···Se (2.552 Å) and N-H···Cl (2.440 Å and 2.613 Å) hydrogen bonding interactions. Single crystal X–ray diffraction shows that $Cr_2Se_2(en)_4Br_2$ is isostructural to $Cr_2Se_2(en)_4Cl_2$.

The crystal structure for $Cr_2S_2(en)_4Cl_2$ was refined using high–resolution synchrotron PXRD (Fig. S6). Rietveld refinement confirmed it to isostructural to the Se dimers discussed above. The unit cell of the Cr_2S_2 dimer is smaller than its selenium counterpart particularly along [100] axis due to the smaller atomic radii of sulfur (Table 1). The Cr_2S_2 core is less distorted than that of Se compound, and Cr–S distances vary from 2.334(3)–2.343(2) Å while the Cr–Cr distance across the core being 3.304(3) Å (Table 2). The respective ∡ S–Cr–S and ∡ Cr–S–Cr measure to

be 90.08(9)° and 89.92(9)° giving rise to a rather shrunken core. The Cr–N bond distances completing the octahedral geometry range from 2.109(3)–2.201(4) Å.

Table 2. Selected bond distances in the crystal structures of $Cr_2Se_2(en)_4Cl_2$, $Cr_2Se_2(en)_4Br_2$, $Cr_2S_2(en)_4Cl_2$, and $Cr_2Se_8(en)_4$ dimers.

Bond	Distance (Å)	Bond	Distance (Å)
$Cr_2Se_2(en)_4Cl_2$		**$Cr_2Se_8(en)_4$**	
Cr1 – Cr1	3.540(3)	Cr1 – Cr1	5.286(8)
Cr1 – Se1	2.460(1)	Cr1 – Se1	2.509(6)
Cr1 – Se1	2.484(2)	Cr1 – Se7	2.505(8)
Cr1 – N1	2.108(6)	Cr2 – Se4	2.490(7)
Cr1 – N2	2.100(7)	Cr2 – Se8	2.522(6)
Cr1 – N3	2.081(7)	Se1 – Se2	2.3672(6)
Cr1 – N4	2.151(7)	Se2 – Se3	2.340(8)
$Cr_2Se_2(en)_4Br_2$		Se4 – Se5	2.358(7)
Cr1– Cr1	3.538(1)	Se5 – Se6	2.352(6)
Cr1 – Se1	2.463(6)	Se7 – Se8	2.379(7)
Cr1 – Se1	2.484(7)	Cr1–N1	2.073(2)
Cr1 – N1	2.091(3)	Cr1–N2	2.105(3)
Cr1 – N2	2.159(2)	Cr1–N3	2.097(2)
Cr1 – N3	2.119(3)	Cr1–N4	2.090(2)
Cr1 – N4	2.096(3)	Cr2–N5	2.078(3)
$Cr_2S_2(en)_4Cl_2$		Cr2–N6	2.123(3)
Cr1– Cr1	3.304(3)	Cr2–N7	2.104(2)
Cr1 – S1	2.343(2)	Cr2–N8	2.080(3)
Cr1 – S1	2.334(3)		
Cr1 – N1	2.109(3)		
Cr1 – N2	2.115(4)		
Cr1 – N3	2.201(4)		
Cr1 – N4	2.116(5)		

Crystal structure of $Cr_2Se_8(en)_4$ phase

$Cr_2Se_8(en)_4$ crystalizes in space group *C*2/*c*, lattice parameters are given in Table 1. Unlike the closed Cr_2Se_2 core of $Cr_2Se_2(en)_4X_2$, Cr atoms in $Cr_2Se_8(en)_4$ are connected to each other with one –Se–Se– bridge. Each chromium atom is also connected to an arm of three selenium atoms, –Se–Se–Se, protruding like the claws of a crustacean (Fig. 3A). Crystal structure of a single unit with ADPs is shown in Fig. S9. Chromium maintains its six coordinated geometry with four N atoms from two ethylenediamine molecules completing the metal coordination. Cr–N bond distances ranging from 2.073(2) – 2.123(3) Å, along with varying Cr–Se bonds makes the geometry around chromium be of a distorted octahedron. Every Se–Se bond is different with an average of 2.5 Å (Table 2), so that the selenium arms are not identical. Interatomic bond distance between chromium atoms has increased to 5.286(8) Å due to the extra bridging selenium atom.

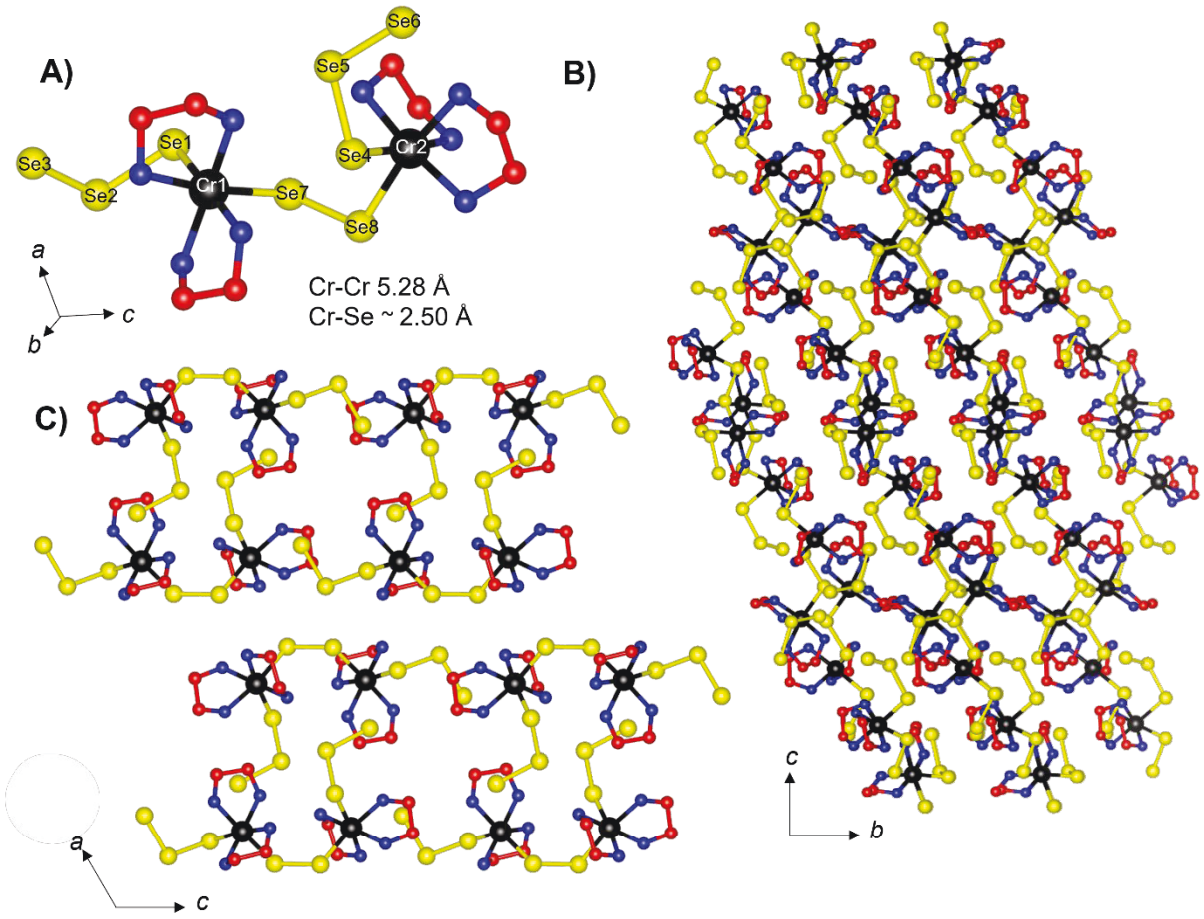

Figure 3. Crystal structure of $Cr_2Se_8(en)_4$ **A)** Structure of one molecule of $Cr_2Se_8(en)_4$ **B) – C)** General view in [100] and [010] crystallographic directions. Cr: black; Se: yellow; N: blue; C: red. All hydrogen atoms are omitted for clarity.

The individual fragments are arranged in such a manner that its protruding selenium arms are pointed towards the Cr–*en* chelate rings of the neighboring fragments (Fig. 3B and 3C). This arrangement creates a pseudo two dimensional ladder–like structure where the entwined chains propagate along [001] direction (Fig. 3C). The superficial ladders consist of Cr–Se backbones appearing as rails connected by the selenium arms acting as steps and the 'ladders' look well separated from one another. Since $Cr_2Se_8(en)_4$ is a neutral molecule, chromium holds a +3 charge while Se2 and Se5 are neutral, leaving rest of the Se atoms at a –1 charge.

Magnetic Properties

In the crystal lattices containing the dimeric transition metal complexes, the intermolecular interactions are typically very weak, precluding long-range magnetic ordering. In turn, the *intra*dimer magnetic coupling can be quite strong resulting in significant deviation from paramagnetic Curie-Weiss behavior at temperatures when coupling strength is comparable to thermal energy. The strength of the magnetic coupling *J* depends on the distance between the metal centers as well as on the type of the bridging ligand which may facilitate magnetic super exchange

interactions.[59] Metal dimers with antiferromagnetic coupling exhibit a maximum of their magnetic susceptibility (χ) versus temperature dependence. With increasing antiferromagnetic interaction, the temperature of that maximum increases, while its height decreases.[59-61] Also, the maximum becomes broader with increasing interaction energy. On the other hand, ferromagnetic dimers show maximum of their χT vs T dependence.

First, to ensure phase purity of the $Cr_2Q_2(en)_4X_2$ samples, isothermal magnetization, M(H) studies were conducted at 2 K, 50-75 K and at 300 K. For all four compounds, M(H) data under an applied field of 0-1.0 T show that the samples are clean of ferro- or ferri- magnetic impurities (Fig. S10). Based on this result, magnetic susceptibility measurements were conducted under an applied field of 1000 Oe (Fig. 4), to be in the linear limit of M(H) even at lowest temperatures.

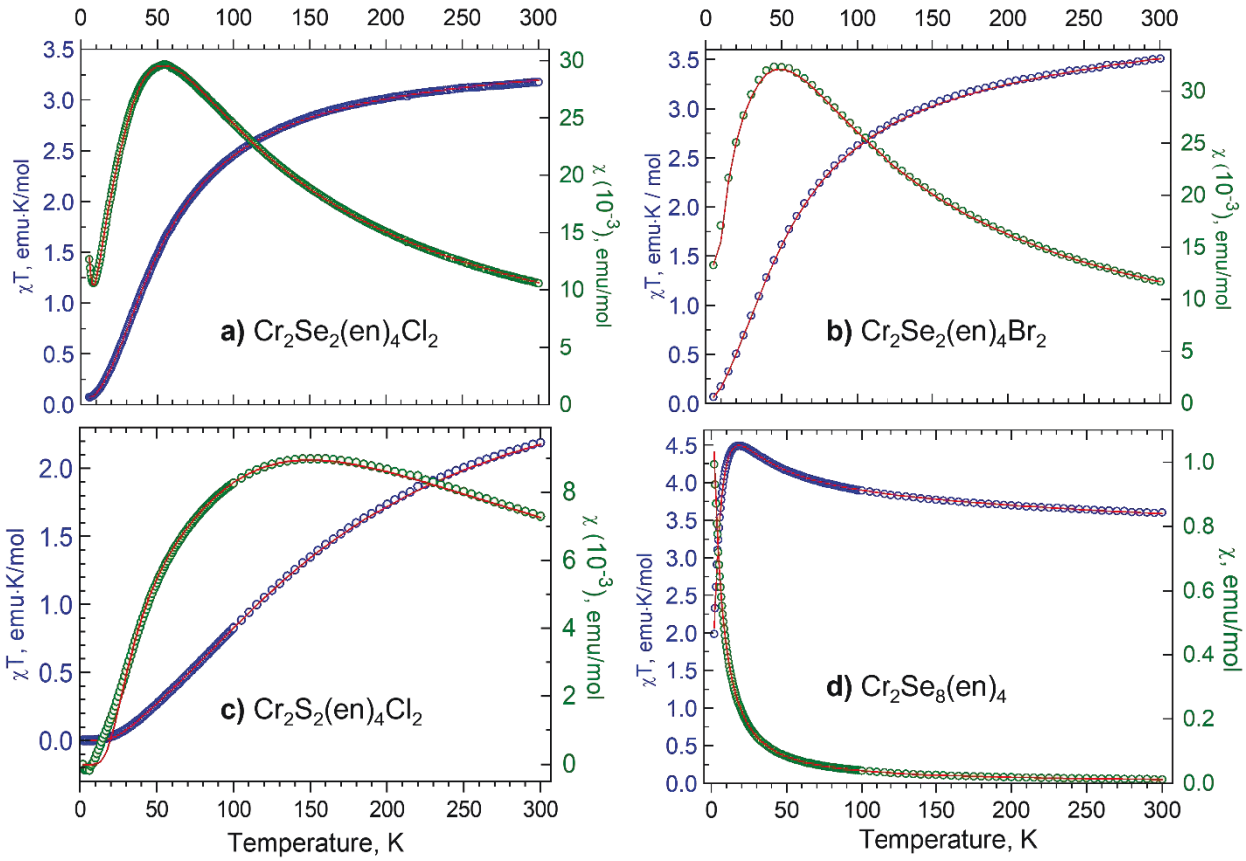

Figure 4. The experimental χ vs T (green) and χT vs T (blue) data measured at the magnetic field of 1000 Oe for **a)** $Cr_2Se_2(en)_4Cl_2$, **b)** $Cr_2Se_2(en)_4Br_2$, **c)** $Cr_2S_2(en)_4Cl_2$ and **d)** $Cr_2Se_8(en)_4$. The red plots were simulated using a spin Hamiltonian including the biquadratic exchange given in Table 3.

The temperature dependence of the magnetic susceptibility of $Cr_2Se_2(en)_4Cl_2$, synthesized from elemental Cr powder suggests the presence of a dimer with moderately strong antiferromagnetic coupling. Similar magnetic properties were observed for the sample of $Cr_2Se_2(en)_4Cl_2$, made from soluble $CrCl_3{\cdot}6H_2O$ with no ferro- or ferrimagnetic impurity. Magnetic characterization of $Cr_2Se_2(en)_4Cl_2$ indicates an antiferromagnetic exchange in the Cr dimer

emphasized in the peak in the χ vs T curve around 55 K, with a maximum χ value of ~30 × 10^{-3} emu/mol (note that the scales in the plots are adjusted to clearly show the of low temperature features), followed by a sharp decrease in susceptibility at lower temperatures (Fig. 4a). The χT vs T plot exhibits a steady nonlinear decline down to ~75 K and a subsequent drop over a short temperature range in accordance with antiferromagnetic interactions in the Cr_2Se_2 dimer (Fig 4a). Isothermal magnetization agrees with the antiferromagnetic coupling where low values of magnetization were observed at 2 K where it reaches a saturated value of 0.1 μ_B under 6 T (Fig. 5a).

Magnetic characterization of $Cr_2Se_2(en)_4Br_2$ demonstrated a similar trend like its chloride counterpart. The χ vs T curve, with a maximum value of ~32 × 10^{-3} emu/mol at 45 K (Fig. 4b) is characteristic for antiferromagnetic coupling and displays nonlinear decrease with decreasing temperature (Fig. 4b). Isothermal magnetization displays the lowest values of magnetization at 2 K (Fig. 5b).

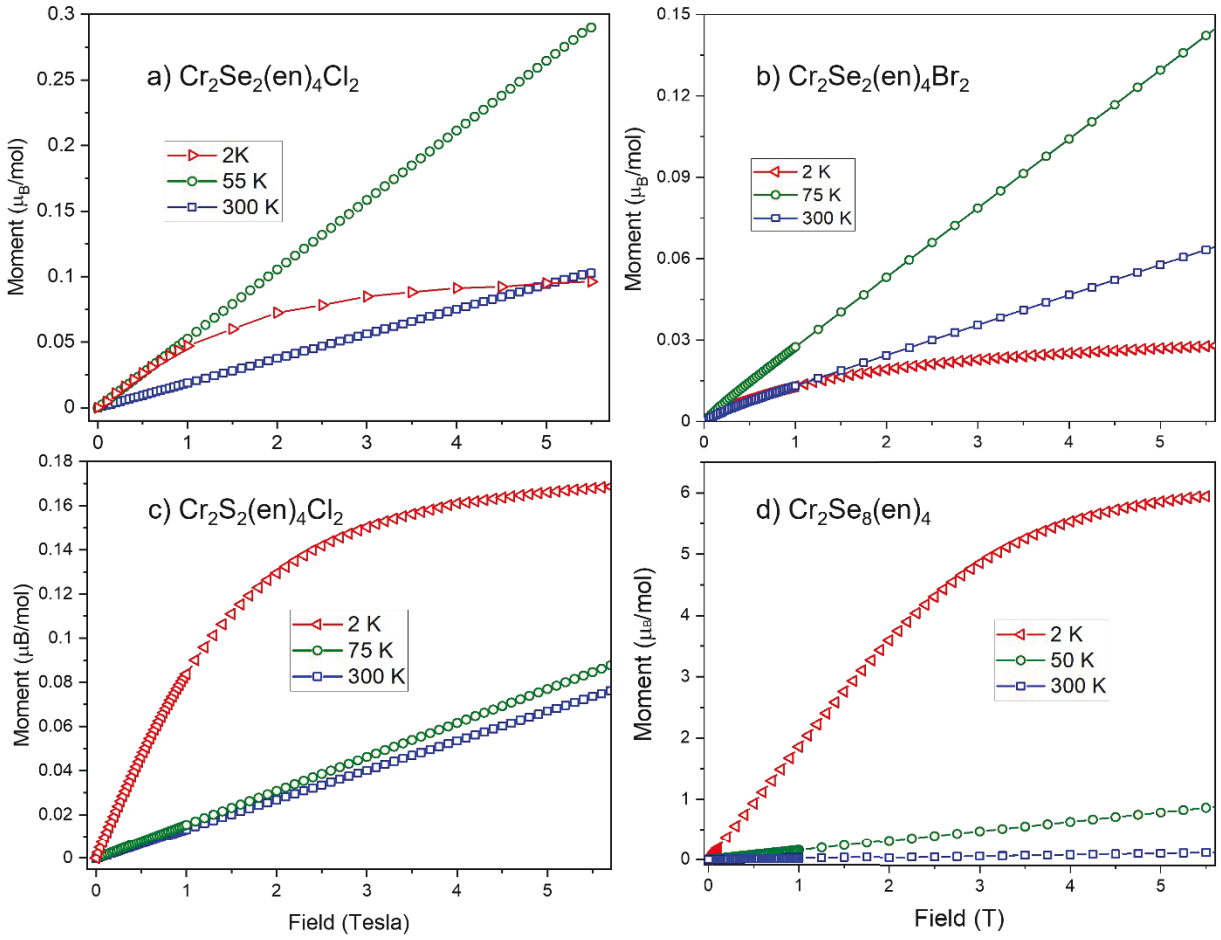

Figure 5. Isothermal magnetization (M vs H) curves for a) $Cr_2Se_2(en)_4Cl_2$, b) $Cr_2Se_2(en)_4Br_2$, c) $Cr_2S_2(en)_4Cl_2$ and d) $Cr_2Se_8(en)_4$ compounds measured at different temperatures.

Magnetic studies for $Cr_2S_2(en)_4Cl_2$ were conducted on samples synthesized from $CrCl_3 \cdot 6H_2O$ and thiourea. Overall susceptibility and magnetization for the $Cr_2S_2(en)_4Cl_2$ dimer is

significantly lower compared to the $Cr_2Se_2(en)_4X_2$ dimers. The χ vs T plot displayed a broad maximum centered around 150 K indicating strong antiferromagnetic coupling between Cr centers followed by a steady reduction in susceptibility down to 5 K (Fig. 4c). The maximum χ value of ~9.0×10^{-3} emu/mol is only 1/3 of the maximum χ of the selenium analogue. It is important to note that the onset of the broad maximum takes place at a higher temperature for Cr_2S_2 dimers than both Cr_2Se_2 dimers. The χT vs T plot shows a gradual nonlinear decrease with decreasing temperatures which is typical for antiferromagnetically coupled dimers (Fig. 4c). Isothermal magnetization is at a maximum at 2 K and reaches a saturation of 0.2 μ_B under 6 T (Fig. 5c).

For $Cr_2Se_8(en)_4$ finely ground crystal chunks hand-picked from the sample were used for magnetic studies. Magnetic susceptibility shows no magnetic ordering down to 1.8 K under 1000 Oe applied field (Fig. 4d). The increasing χT product with a maximum at ~30 K upon cooling, indicates ferromagnetic interactions between Cr atoms connected by the Se_2 bridge (Fig. 4d). A sharp drop in χT values below 18 K is due to the weak antiferromagnetic interaction between the dimer molecules. The field dependence of magnetization confirms the ferromagnetic nature of the Cr–Cr interactions; the highest magnetization was observed at lowest temperature, 2 K (Fig. 5d). At the applied magnetic field of 5.5 T, the saturation magnetization of 6 μ_B/f.u. was achieved as expected for two Cr^{3+} ions with aligned spins.

Magnetic exchange calculations

Exchange interactions between two Cr^{3+} ions with spin $S = 3/2$ give rise to four states of coupled spin $\hat{\boldsymbol{S}} = \hat{\boldsymbol{S}}_1 + \hat{\boldsymbol{S}}_2$, with the total S quantum numbers 0, 1, 2 and 3.[8,11,34-45,59-64] The magnetic properties of such dimeric systems are usually described by the Heisenberg–Dirac–VanVleck (HDVV) Hamiltonian:

$$\boldsymbol{H} = J\,\hat{\boldsymbol{S}}_1 \cdot \hat{\boldsymbol{S}}_2 \qquad (1)$$

where $\hat{\boldsymbol{S}}_1$ and $\hat{\boldsymbol{S}}_2$ are the spin operators on centers 1 and 2. A positive J corresponds in this notation to antiferromagnetic interactions. (Note that other notations have also been used in literature, like $-J\,\hat{\boldsymbol{S}}_1 \cdot \hat{\boldsymbol{S}}_2$ and $-2J\,\hat{\boldsymbol{S}}_1 \cdot \hat{\boldsymbol{S}}_2$). In our case, attempts of fitting the magnetic susceptibility by using energies resulting from Eq. 1 were unsuccessful indicating a need of the inclusion of the biquadratic exchange term $j(\hat{\boldsymbol{S}}_1 \cdot \hat{\boldsymbol{S}}_2)^2$. Interestingly, the need to include the biquadratic exchange often arises in studies on coupled Cr^{3+} pairs,[35,36,38,40,45,62–66] while this term is not needed in other d^3–d^3 dimers.[8] It is associated with the effect of the exchange interaction on the metal–metal distance and is correlated with the elastic stiffness coefficient.[65] This is referred to as the "exchange striction" and is expected to produce positive j values in the notation used in this paper.[65] (Note that ref. 65 uses a different sign convention) This effect is particularly strong in the case of Cr dimers having 90° Cr–X–Cr bridges,[65] like in reported here Cr_2X_2 cores. The effects of the biquadratic exchange on two dimensional magnets have been investigated recently.[66]

The corrected spin Hamiltonian is

$$\hat{\boldsymbol{H}} = J\hat{\boldsymbol{S}}_1\hat{\boldsymbol{S}}_2 - \boldsymbol{j}\left(\hat{\boldsymbol{S}}_1\hat{\boldsymbol{S}}_2\right)^2 \qquad (1a)$$

The magnetic susceptibility per one mole of the dimer can be calculated from

$$\chi = \frac{N\mu_B^2 g^2 \sum_{S=0}^{3}(2S+1)(S+1)S\exp\left(-\frac{E_S}{k_B T}\right)}{3k_B T \sum_{S=0}^{3}(2S+1)\exp\left(-\frac{E_S}{k_B T}\right)} + 2TIP \qquad (2)$$

In (2) the energies E_S calculated either according to spin Hamiltonian (1) or (1a) can be used (*TIP*: temperature independent parameter). This method works well provided that the energy splits within the S states are small compared to the thermal energy, $k_B T$. In our cases, the zero–field splitting effects are small (see below), and the approach described above should work properly. At high fields, the Zeeman splitting becomes comparable or larger than the thermal energy at low temperatures. To account for such effects, a full "microscopic" spin Hamiltonian (3) was used.

$$\begin{aligned}\hat{\boldsymbol{H}} &= J\hat{\boldsymbol{S}}_1\hat{\boldsymbol{S}}_2 - \boldsymbol{j}\left(\hat{\boldsymbol{S}}_1\hat{\boldsymbol{S}}_2\right)^2 + \mu_B\boldsymbol{B}\{\boldsymbol{g}_1\}\hat{\boldsymbol{S}}_1 + \mu_B\boldsymbol{B}\{\boldsymbol{g}_2\}\hat{\boldsymbol{S}}_2 \\ &+ D_{Cr}\left\{\hat{\boldsymbol{S}}_{z1}^2 - \tfrac{1}{3}S(S+1)\right\} + E_{Cr}\left(\hat{\boldsymbol{S}}_{x1}^2 - \hat{\boldsymbol{S}}_{y1}^2\right) + D_{Cr}\left\{\hat{\boldsymbol{S}}_{z2}^2 - \tfrac{1}{3}S(S+1)\right\} + E_{Cr}\left(\hat{\boldsymbol{S}}_{x2}^2 - \hat{\boldsymbol{S}}_{y2}^2\right) \qquad (3) \\ &+ D_{12}\left\{\hat{\boldsymbol{S}}_{z1}\hat{\boldsymbol{S}}_{z2} - \frac{1}{3}\hat{\boldsymbol{S}}_1\hat{\boldsymbol{S}}_2\right\} + E_{12}(\hat{\boldsymbol{S}}_{x1}\hat{\boldsymbol{S}}_{x2} - \hat{\boldsymbol{S}}_{y1}\hat{\boldsymbol{S}}_{y2})\end{aligned}$$

Parameters D_{Cr} and E_{Cr} describe the zero–field splitting on each d^3 ion, while D_{12} and E_{12} describe the contribution to zero–field splitting caused by the anisotropic metal–metal interactions. The reported here di–bridged dimers are centrosymmetric and using the same D_{Cr} and E_{Cr} for both atoms is justified. Although this is not true for the ferromagnetic mono–bridged complex, the same approach was used since there is no way to determine these parameters separately for each ion. The spin Hamiltonian (3) operates within the set of 16 $|m_{S1},m_{S2}>$ functions in a d^3–d^3 dimer. The energy levels in the magnetic fields calculated using spin Hamiltonian (3) are presented in Figure S11. To calculate the magnetic susceptibility, the fundamental equation employed was:

$$\chi_{dim} = -\frac{N_A \sum_i \frac{\partial E_i}{\partial B}\sum_i \exp\left(-\frac{E_i}{kT}\right)}{B \sum_i \exp\left(-\frac{E_i}{kT}\right)} + 2TIP \qquad (4)$$

The 16 energies E_i were calculated by diagonalizing spin Hamiltonian (3). The derivatives with respect to the magnetic field B, $\frac{\partial E_i}{\partial B}$, were evaluated by calculating the energies 5 Gauss below and 5 Gauss above the applied field of the SQUID magnetometer. Trace paramagnetic contamination present in the antiferromagnetic dimers was considered by modifying Eq 4:

$$\chi = (1-x)\chi_{dim} + 2x\frac{N\mu_B^2 g^2 15}{3k_B T\ 4} \qquad (5)$$

where x is the fraction of a $S = 3/2$ impurity. Finally, the susceptibility was corrected for the interactions with neighboring dimers, zJ as

$$\chi_{corr} = \frac{\chi}{1 - \chi zJ/N\mu_B^2 g^2} \qquad (6)$$

χ_{corr} of Eq. (6) was fitted to the experimental data. Parameters D_{Cr} were fixed to the values found from EPR. Parameters E_{Cr}, D_{12} and E_{12} were neglected in calculating the magnetic susceptibility.

The magnetic fitting results are presented in Table 3 together with the HFEPR results. All three di–bridged dimers exhibit antiferromagnetic interactions while the single–bridged complex $Cr_2Se_8(en)_4$ is ferromagnetic. The biquadratic exchange constants are positive with magnitudes ranging from ~6% to ~14% of the respective J values.

High–Field EPR spectra

The spin Hamiltonian parameters can in principle be determined in each coupled spin state, as was done in ref 45. Unfortunately, the spectra observed in this work did not contain as much information. $Cr_2Se_2(en)_4Cl_2$ produced the best EPR spectra in this series. A characteristic pattern of signals due to the coupled spin state $S = 1$, with a prominent "forbidden" $\Delta m_S = 2$ transition, could be observed over a narrow temperature range and was best seen at 10 K. (Figs. 6, 7).

Table 3. Spin Hamiltonian parameters found from the magnetic and HFEPR data. The Cr–Cr bond distances are indicated in parentheses. J: exchange constant, j: biquadratic exchange constant, g_x, g_y, g_z: g-factor components, D and E: contribution to zero–field splitting caused by the anisotropic metal–metal interactions, D_{Cr}, E_{Cr}: zero–field splitting on each d^3 ion.

Complex	**Magnetism data**			**HF-EPR data**					
	J, cm^{-1}	j, cm^{-1}	g_x	g_y	g_z	D, cm^{-1}	E, cm^{-1}	D_{Cr}, cm^{-1}	E_{Cr}, cm^{-1}
$Cr_2Se_2(en)_4Cl_2$	15.1 (3.54 Å)	2.1	1.993	1.993	2.002	1.019[a]	0.112[a]	–0.4	0.0
$Cr_2Se_2(en)_4Br_2$	17.7 (3.54 Å)	1.0	1.993	1.993	2.003	1.05[a]	0.159[a]	–0.4	–0.02
$Cr_2S_2(en)_4Cl_2$	49.0 (3.30 Å)	4.6	1.991	1.991	1.989	0.340[a]	0.075[a]	–0.09	0.02
$Cr_2Se_8(en)_4$	–6.1 (5.27 Å)	0.85	1.997	2.00	1.975	0.046[b]	0.0075[b]	-	-

[a] Parameters in the $S = 1$ state. [b] Parameters in the $S = 3$ state. The estimated errors are few units in the last reported digit.

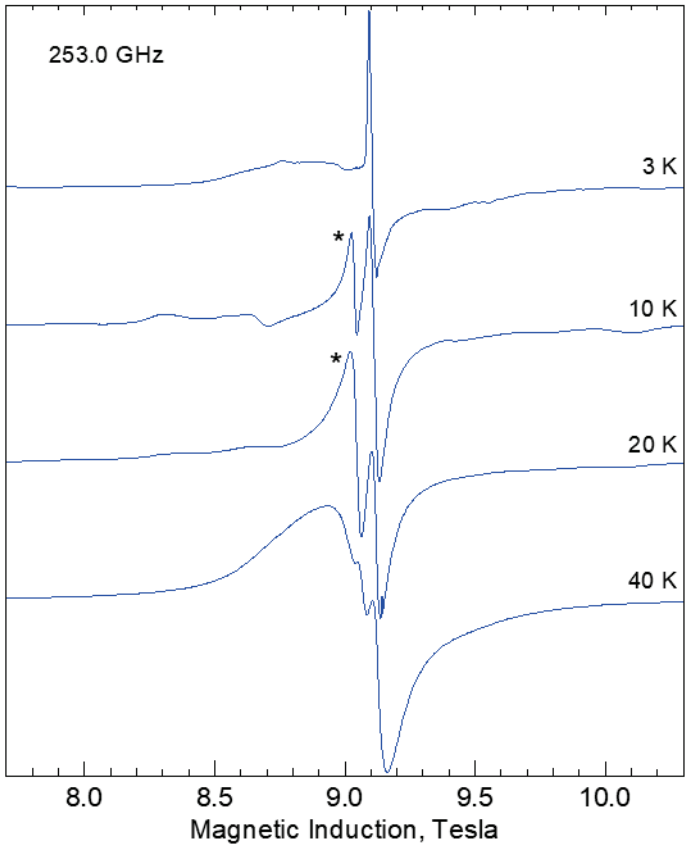

Figure 6. Temperature dependence of the $\Delta M_S = 1$ signals in the 253 GHz spectra of $Cr_2Se_2(en)_4Cl_2$. The asterisk indicates a possible resonance in the $S = 2$ state. The sharp central feature located at $g = 1.985$ is probably due to a monomeric Cr^{3+} impurity. See also Figs. 7, S11 and S12.

At temperatures above 30 K (Fig. 6) only a broad signal was observed presumably as a result of fast relaxation between the coupled spin states of $S = 1$, 2, and 3 of the dimer. At 20 K and 10 K, the $S = 2$ and $S = 1$ signals are visible, and their relative intensities change with temperature according to the population of these states, thus the $S = 2$ signal disappears faster than the $S = 1$ signal with lowering the temperature (Fig. S12). No resonances due to the $S = 3$ state could be observed owing to the low population of this state. Both the $S = 1$ and $S = 2$ signals are not seen at 3 K. The resonances still observed at 3 K, cannot therefore be due to the antiferromagnetic dimer. The signal marked with an asterisk in Fig. 6 may belong to the $S = 2$ spectrum, but no other $S = 2$ or $S = 3$ resonances could be identified. This made experimental determination of the spin Hamiltonian parameters of $S = 2$ and $S = 3$ states impossible, and the spin Hamiltonian parameters of only the triplet state ($S = 1$) could be determined. The "giant spin" Hamiltonian used was:

$$\hat{\mathbf{H}}_S = \mu_B \mathbf{B}\{\mathbf{g}_S\}\hat{\mathbf{S}} + D_S\left\{\hat{\mathbf{S}}_z^2 - \tfrac{1}{3}S(S+1)\right\} + E_S\left(\hat{\mathbf{S}}_x^2 - \hat{\mathbf{S}}_y^2\right) \quad (7)$$

Parameters D_S and E_S are different in different coupled spin states (that is $S = 1$, 2, and 3) of a dimer. These parameters contain contributions due to zero-field splitting on separate $S = 3/2$ ions (D_{Cr}, E_{Cr}) and contributions due to the anisotropic interactions between the ions (D_{12}, E_{12}). In a d^3–d^3 dimer case, the relations between the parameters of the "giant spin" Hamiltonian (7) and the "microscopic" Hamiltonian (3) are[8,11,36,40,43,45]

$$D_{S=1} = 1.7\, D_{12} - 2.4 D_{Cr}$$

$$D_{S=2} = 0.5\, D_{12} \qquad (8)$$

$$D_{S=3} = 0.3\, D_{12} + 0.4 D_{Cr}$$

The same coefficients relate the coupled–spin E_S parameters to E_{12} and E_{Cr}, and the limitations of this model were discussed recently.[40]

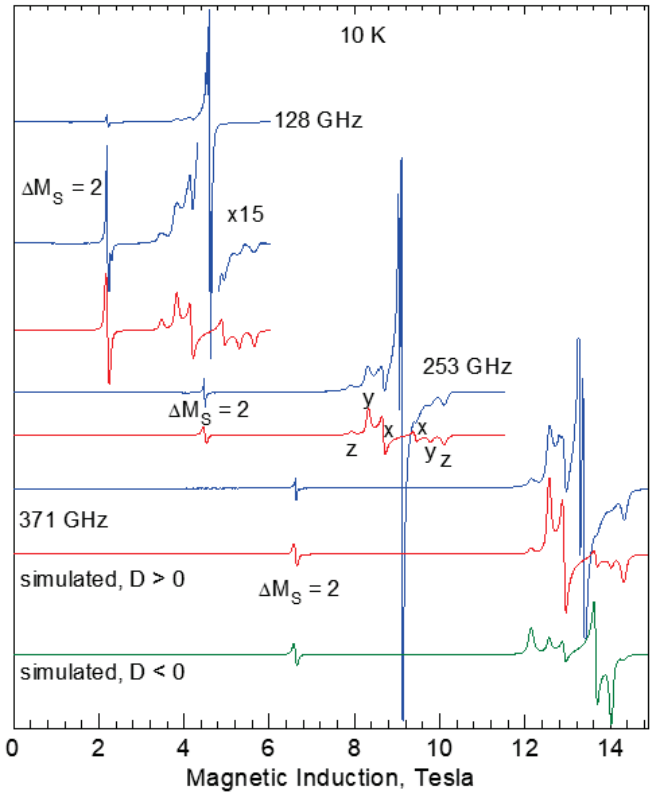

Figure 7. HF EPR spectra of $Cr_2Se_2(en)_4Cl_2$ recorded at 10 K with microwave frequencies as shown. Labels x, y and z designate the orientation of the molecule versus the magnetic field at which these transitions occur. The "forbidden" $\Delta M_S = 2$ feature is marked. The red traces were simulated for $S = 1$ with parameters in Table 3 (D, $E > 0$), the green trace at the bottom was simulated with D and E of the same magnitude, but assumed negative to illustrate the effect of the sign of D.

Spectra shown as red traces in Fig. 7 were simulated using $S = 1$, $g_x = 1.993$, $g_y = 1.993$, $g_z = 2.002$, $D_{S=1} = 1.019$ cm^{-1}, $E_{S=1} = 0.112$ cm^{-1}. The intensity pattern with the high–field "z"

features being stronger than the low–field "z" features, particularly at the highest frequency, while the high–field "x" and "y" features are weaker than their low–field partners, is consistent with positive $D_{S=1}$ (Fig. 7).

Since we know only the parameters of the $S = 1$ state, the determination of D_{Cr}, D_{12} and E_{Cr}, E_{12} cannot be accomplished experimentally. The D_{12} parameter is expected to consist mainly of the magnetic dipole–dipole interaction between the Cr^{3+} ions:

$$D_{12} = -\frac{3\mu_B^2 g^2}{R^3} \qquad (9)$$

where R is the distance between ions. The dipolar contribution to E_{12} is expected to be zero due to very small g anisotropy. With $R = 3.54$ Å, for both $Cr_2Se_2(en)_4Cl_2$ and $Cr_2Se_2(en)_4Br_2$, one obtains D_{12} of –0.12 cm^{-1}. In turn, $D_{S=2}$ of around –0.06 cm^{-1} is expected according to Eq. 8. This is a high estimate because the electron delocalization, which is not considered in Eq. 9, will result in the reduction of the dipole–dipole contribution to D_{12}. Eq. 9 produces a D_{12} equal to –0.14 cm^{-1} for $Cr_2S_2(en)_4Cl_2$, ($R = 3.3$ Å). For the three centrosymmetric dimers $Cr_2Se_2(en)_4Cl_2$, $Cr_2Se_2(en)_4Br_2$, and $Cr_2S_2(en)_4Cl_2$, the "Z" axis of the D_{Cr} tensor is expected to be approximately perpendicular to the Cr_2X_2 plane, while the "Z" axis of the dipolar D_{12} tensor is along the Cr-Cr direction. To apply Eq. 8, in order to estimate D_{Cr} and E_{Cr}, the D_{Cr} and D_{12} tensors must be expressed in the same coordinates, which can be accomplished by rotating the D_{12} tensor by 90° about an axis lying in the Cr_2X_2 plane and perpendicular to the Cr-Cr vector. When doing so, the $D_{12} = -0.12$ cm^{-1}, $E_{12} = 0$ parameter calculated above converts to $D_{12} = 0.06$ cm^{-1} and $E_{12} = -0.06$ cm^{-1}. The D_{Cr} and E_{Cr} values in Table 3 were obtained from these latter D_{12}, E_{12} as well as from $D_{S=1}$, $E_{S=1}$. For $Cr_2Se_8(en)_4$ with the Cr-Cr distance of 5.27 Å, Eq. 9 produces D_{12} of –0.035 cm^{-1}. This is however a non-centrosymmetric system, possibly with different zfs parameters on each Cr^{3+} ion, and the simple procedure described above cannot be applied. We therefore do not attempt to estimate D_{Cr} and E_{Cr} in this case. A more in-depth description of that procedure can be found in refs 8 and 45.

$Cr_2Se_2(en)_4Br_2$ produced spectra very similar to those of $Cr_2Se_2(en)_4Cl_2$ (Fig. 8). Using the "giant spin" approach, as above, the following spin Hamiltonian parameters were found: $g_x = 1.993$, $g_y = 1.993$, $g_z = 2.003$, $D_{S=1} = 1.047$ cm^{-1}, $E_{S=1} = 0.159$ cm^{-1}. The main difference compared to $Cr_2Se_2(en)_4Cl_2$ is a considerably larger E value in the Br species (by a factor of 1.4), resulting in larger spacing between the X and Y features, as seen when Fig. 7 is compared to Fig. 8.

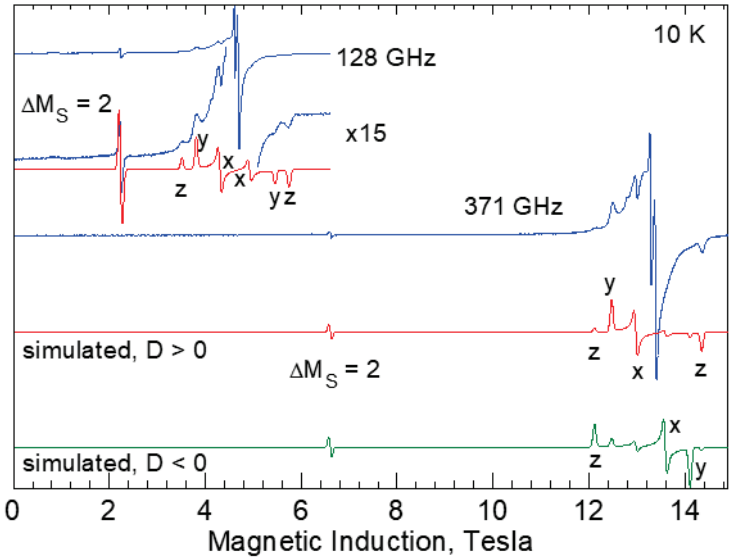

Figure 8. HF EPR spectra of $Cr_2Se_2(en)_4Br_2$ recorded at 10 K with microwave frequencies as shown. Labels x, y and z designate the orientation of the molecule versus the magnetic field at which these transitions occur. The "forbidden" $\Delta M_S = 2$ feature is marked. The red traces were simulated for $S = 1$ with parameters in Table 3 (D, E > 0), the green trace at the bottom was simulated with D and E negative, resulting in an incorrect intensity pattern.

We cannot offer a justification for that difference in E, as the environment of the Cr^{3+} ions and the distance between them are similar in both complexes. The parameters may be affected by the presence of the heavy Br atom with stronger spin–orbit coupling, even if Br is not coordinated to Cr. Similarly, as in $Cr_2Se_2(en)_4Cl_2$, only one feature which may belong to the $S = 2$ state is observed.

$Cr_2S_2(en)_4Cl_2$ spectra are of much lower quality than those of the Se dimers (Fig. 9). The $S = 1$ spectrum can be recognized with the $D_{S=1}$ parameter surprisingly much lower than in the Se bridged compounds. The half–field transition is seen at any microwave frequency, and its position as well as the positions of the 'allowed' transitions in the spectra center can be reproduced using $D_{S=1}$ of 0.34 cm^{-1} and $E_{S=1} = 0.075$ cm^{-1}. A contamination, probably with monomeric Cr^{3+} species is seen at low temperatures (10 K and below) at which the dimer spectrum disappears due to relatively strong antiferromagnetic exchange interactions.

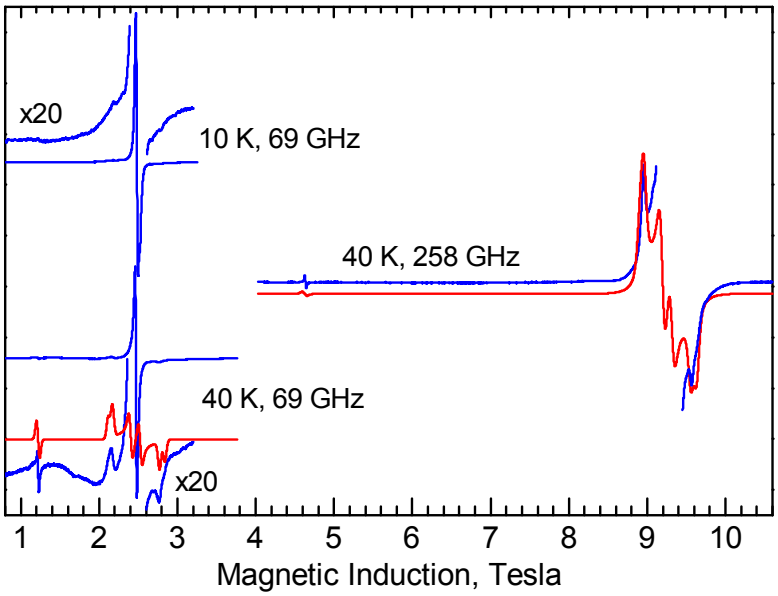

Figure 9. HF EPR spectra of $Cr_2S_2(en)_4Cl_2$. The "forbidden" $\Delta M_S = 2$ feature is located in the 40 K spectra at 1.22 T and 4.63 T, at 69 GHz and at 258 GHz, respectively. The red traces were simulated with parameters in Table 3. A strong central line, which is due to contaminations, was cut off in the 258 GHz plot.

$Cr_2Se_8(en)_4$

The compound exhibits unusually strong relaxation, so that spectra taken at 3 K are significantly different from those taken at 5 K (Fig. 10). With increasing temperature, the outer spectral features move towards the center. Since the complex is ferromagnetic, one should expect an $S = 3$ spectrum at the lowest temperatures. The salient features of the spectra could be tentatively simulated using $S = 3$ and parameters in Table 3, which were determined from the 3 K spectrum. Moreover, an additional weak feature, marked with asterisk in Fig. 11, was seen. That weak feature was observed at a frequency–independent distance from the main spectrum (Fig. 11). The frequency dependence of that resonance allowed to determine a g value of 1.975. Integration of the spectra (not shown) indicates that this feature has a very low intensity compared to the main spectrum.

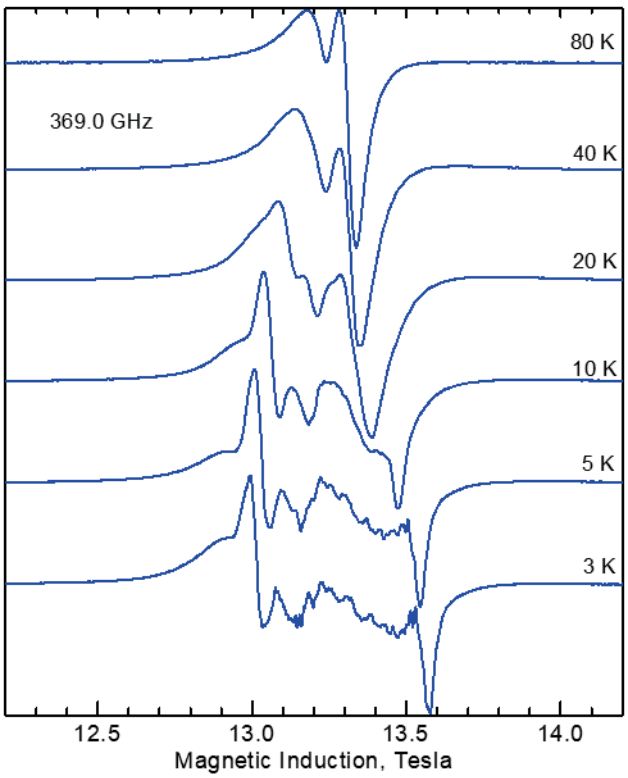

Figure 10. The temperature dependence of the HF-EPR spectra of $Cr_2Se_8(en)_4$.

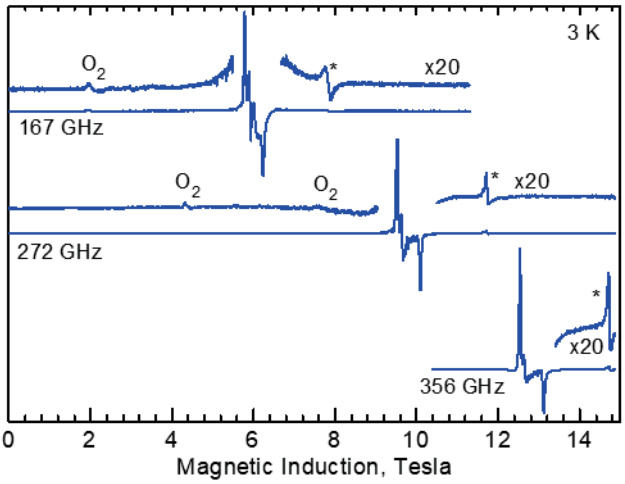

Figure 11. The HF EPR spectra of $Cr_2Se_8(en)_4$ recorded at 3 K and frequencies indicated. Signals due to adsorbed oxygen on the powder sample are marked with O_2, and the additional signals are marked with * in the magnified spectra.

Theoretical calculations

"Broken symmetry" DFT calculations[67–72] were performed to get insight into the metal–metal interactions in the dimers studied here. We have used the free software package ORCA 5.01.[73] DFT calculations used the B3LYP/G, functional in combination with the ma-def2–TZVPP function basis for all atoms. "Broken symmetry" performs first an SCF calculation for a high–spin

state (HS, with $S = 3$), with three spin–up electrons on one metal atom in a dimer and three spin–up electrons on another metal atom. Next, another SCF calculation is done with 3 spin–up electrons on one atom and 3 spin–down electrons on another. This is referred to as a "broken symmetry" state (BS). The J values of the $\hat{H} = J\hat{S}_1\hat{S}_2$ Hamiltonian are then evaluated from the energies of the HS and BS states as $J = \mathbf{2}^{(E_{HS} - E_{BS})} / \left(\langle \hat{\mathbf{S}}^2 \rangle_{HS} - \langle \hat{\mathbf{S}}^2 \rangle_{BS} \right)$, where $\langle \hat{\mathbf{S}}^2 \rangle$ are the average values of the total spin–squared operator in the respective states. It has been reported that the J values derived from such calculations tend to be too large, which is thought to be due to a "self-interaction errors" inherent to DFT.[68,69] An empirical divisor of 2 has often been applied in literature.[68,69] The calculated J values reported below have been corrected using this factor.

The J values of 10.6, 12.6, 44.0, and –14.3 cm^{-1} were obtained for $Cr_2Se_2(en)_4Cl_2$, $Cr_2Se_2(en)_4Br_2$, $Cr_2S_2(en)_4Cl_2$, and $Cr_2Se_8(en)_4$, respectively. When compared to the experimental magnitudes (15.1, 17.7, 49.0 and –6.1 cm^{-1}), extracted from the magnetic data, one can see that the success is rather moderate, particularly in the case of $Cr_2Se_8(en)_4$. The trends in magnitude and sign of J were properly reproduced, but the quantitative agreement is poor. This problem may be due to the presence of heavy bridging atoms. The antiferromagnetic character of the exchange interaction depends on the overlap of the magnetic orbitals of two ions. The magnetic orbitals and their overlap integrals are shown in Figs. 12 and 13. The orbital plots for the Se and S–bridged complexes reveal the overall stronger delocalization of the Cr orbitals onto the S bridge than onto the Se bridge and larger overlap integrals of the magnetic orbitals in the S case, leading to much stronger antiferromagnetic exchange in the S–bridged species (Fig. 12). This explains the reason behind generally low χ values observed for Cr_2S_2 dimer when compared to that of Cr_2Se_2 dimers in their respective χ vs T plots.

The $Cr_2Se_8(en)_4$ complex is not comparable to the other ones because of the different bridge geometry. The delocalization of the magnetic orbitals onto the bridging Se atoms is very small compared to the cases above (Fig. 13). A weak overlap of the magnetic orbitals, one order of magnitude smaller than in the $[Cr_2Q_2(en)_4]^{2+}$ species, results in the weak ferromagnetic exchange interactions.

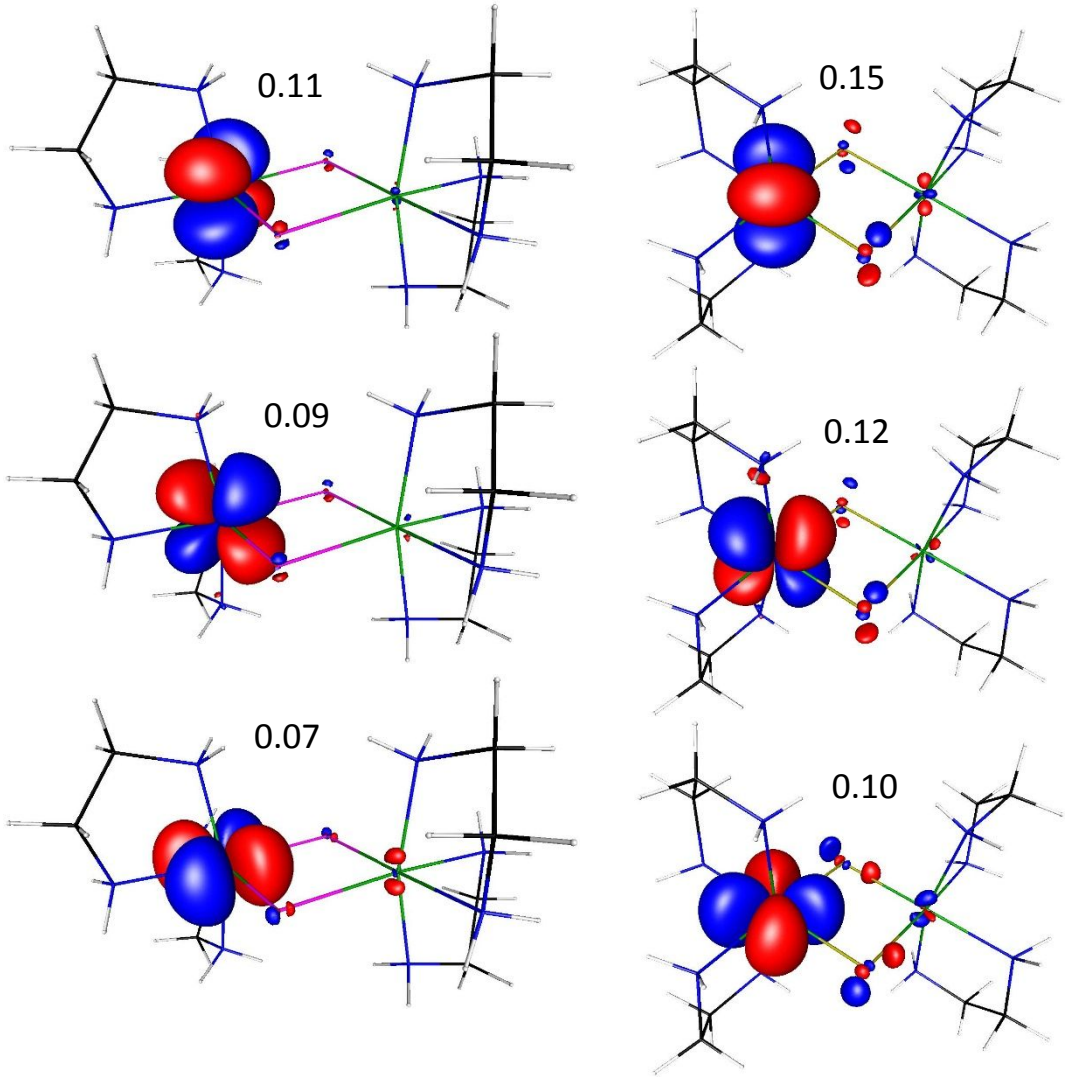

Figure 12. Magnetic orbitals ("corresponding orbitals", "uco" in the ORCA software) in $Cr_2Se_2(en)_4^{2+}$ (left) and in $Cr_2S_2(en)_4^{2+}$ (right). Note that identical magnetic orbitals exist on the other Cr^{3+} ion in each case. The orbitals are shown at the 0.04 isosurface value. The overlap integrals of the plotted orbitals with their partners located on another Cr^{3+} ion are indicated.

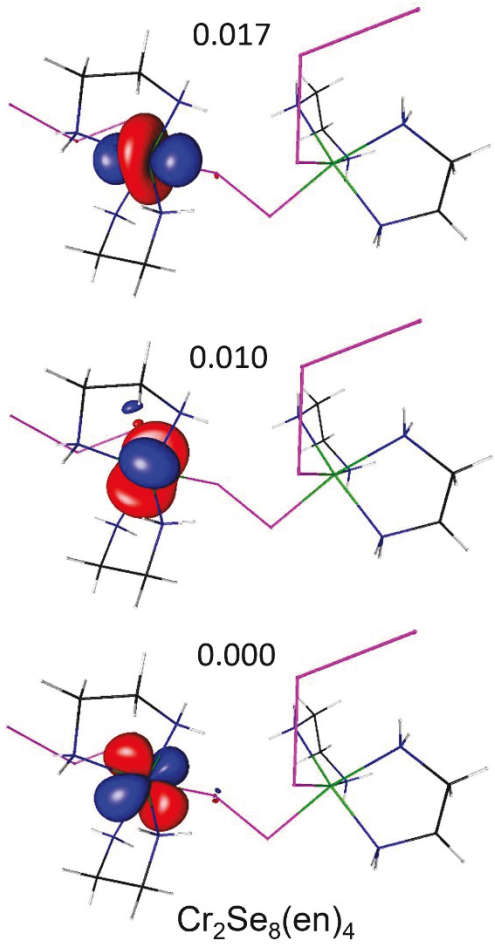

Figure 13. Magnetic orbitals in $Cr_2Se_8(en)_4$. Note that identical magnetic orbitals exist on the other Cr^{3+} ion in each case. The orbitals are shown at the 0.04 isosurface value. The overlap integrals are indicated.

An attempt was also made to calculate the ZFS parameters (D_{Cr}, E_{Cr}) of the local quartet ground states using the state–averaged CASSCF method as implemented in the ORCA software.[74–76] The calculations used the B3LYP/G functional and def2–TZVPP function basis augmented by the def2–TZVPP/C diffuse functions and were performed on molecules in which one of the Cr^{3+} ions was substituted by the diamagnetic Ga^{3+} ion. These calculations were unsuccessful, possibly because of the heavy atoms present in our systems, failing to predict both the magnitude of *D* and its trend in the Se–bridged versus the S–bridged complexes, and will therefore not be described in detail here.

Conclusions

$Cr_2Q_2(en)_4X_2$ (*Q*: S, Se; *X*: Br, Cl; *en*: ethylenediamine) dimer compounds have been synthesized by low temperature solvothermal synthesis free from any oxygen containing ligands or reducing agents. The Se bridges connecting the Cr(III) ions in Cr_2Se_2 square core mediate magnetic exchange between the metal centers and give rise to moderate (Cr_2Se_2 core) or strong

(Cr_2S_2 core) antiferromagnetic interactions. Substituting Se for S resulted a shorter Cr–Cr separation in the dimer and a significant increase in the strength of magnetic coupling, preserving the antiferromagnetic type of interactions as revealed by magnetic and EPR studies. Finally, replacing monoatomic Se bridges with diatomic Se–Se bridge in the structure of neutral $Cr_2Se_8(en)_4$ resulted in altering the type of exchange from antiferromagnetic to ferromagnetic one. The biquadratic exchange effects were observed. The sign of the biquadratic exchange constant *j* suggests that this interaction is due to the exchange striction effects.[65] Reported zero–dimensional dimers are important as discrete molecular building blocks which can be used to form extended structures with tunable magnetic properties.

Funding

This research was supported by National Science Foundation DMR-2003783 grant to KK. This research used the resources at the beamline 17-BM and the mail-in program at the beamline 11-BM-B at Advanced Photon Source at Argonne National Laboratory, supported by the U. S. Department of Energy, Office of Science, Office of Basic Energy Sciences, under Contract No. DE–AC02–06CH11357. Magnetic characterization performed by R.A.R. and P.C.C. were supported by the Ames Laboratory, the US Department of Energy, Office of Science, Basic Energy Sciences, Materials Science and Engineering Division under contract No. DE-AC02-07CH11358. An EPR portion of this work was performed at the National High Magnetic Field Laboratory, which is supported by the National Science Foundation Cooperative Agreement No. DMR–1644779 and the State of Florida.

Acknowledgements

We are thankful to the beamline scientists Dr. Andrey Yakovenko, Dr. Wenqian Xu, (17-BM) and Dr. Saul Lapidus (11-BM) at the APS ANL for their support in conducting the synchrotron experiments. Authors would like to thank Dr. Warren Straszheim and Dr. Shannon Lee for help with SEM/EDS data collection as well as to Dr. Dinesh Amarasinghe for help with the Rietveld refinement.

Supporting Information

SEM and optical mages, table containing a list of synthesis reactions, experimental and theoretical PXRD patterns, 17-BM contour plots, Rietveld refinement data, crystal structures showing ADP and isothermal magnetization curves are included.

References

(1) Bleaney B.; Bowers K. D. Anomalous Paramagnetism of Copper Acetate. *Proc. R. Soc. Lond. A.* **1952**, *214*, 451–465.

(2) Ozarowski, A. The Zero-Field-Splitting Parameter D in Binuclear Copper(II) Carboxylates Is Negative. *Inorg. Chem.* **2008**, *47*, 9760–9762.

(3) Maurice, R.; Sivalingam, K.; Ganyushin, D.; Guihéry, N.; Graaf, C. de; Neese, F. Theoretical Determination of the Zero-Field Splitting in Copper Acetate Monohydrate. *Inorg. Chem.* **2011**, *50*, 6229–6236.

(4) Reger, D. L.; Pascui, A. E.; Foley, E. A.; Smith, M. D.; Jezierska, J.; Wojciechowska, A.; Stoian, S. A.; Ozarowski, A. Dinuclear Metallacycles with Single M-X-M Bridges (X = Cl^-, Br^-; M = Fe(II), Co(II), Ni(II), Cu(II), Zn(II), Cd(II)): Strong Antiferromagnetic Superexchange Interactions. *Inorg. Chem.* **2017**, *56*, 2884–2901.

(5) Klingele, J.; Dechert, S.; Meyer, F. Polynuclear Transition Metal Complexes of Metal···Metal-Bridging Compartmental Pyrazolate Ligands. *Coord. Chem. Rev.* **2009**, *253*, 2698–2741.

(6) Casey, C. P.; Audett, J. D. Synthesis and Reactivity of Saturated Hydrocarbon-Bridged Dinuclear Complexes. *Chem. Rev.* **1986**, *86*, 339-352.

(7) Holton, J.; Lappert, M. F.; Pearce, R.; W Yarrow, P. I. Bridged Hydrocarbyl or Hydrocarbon Binuclear Transition-Metal Complexes: Classification, Structures, and Chemistry. *Chem. Rev.* **1983**, *83*, 135–201.

(8) Premužić, D.; Hołyńska, M.; Ozarowski, A.; Pietzonka, C.; Roseborough, A.; A. Stoian, S. Model Dimeric Manganese(IV) Complexes Featuring Terminal Tris-Hydroxotetraazaadamantane and Various Bridging Ligands. *Inorg. Chem.* **2020**, *59*, 10768–10784.

(9) Delfs, C. D.; Stranger, R. Oxidation State Dependence of the Geometry, Electronic Structure, and Magnetic Coupling in Mixed Oxo- and Carboxylato-Bridged Manganese, Dimers. *Inorg. Chem.* **2001**, *40*, 3061–3076.

(10) Summerville, R. H.; Hoffmann, R. Tetrahedral and Other M_2L_6 Transition Metal Dimers. *J. Am. Chem. Soc.* **1976**, *98*, 7240–7254.

(11) Hogni Weihe, H.; Gudel, H. U. Magneto-Structural Correlations in Linear and Bent Oxo-Bridged Transition-Metal Dimers: Comparisons, Interpretations, and Predictions of Ground-State Magnetic Properties. *J. Am. Chem. Soc.* **1998**, *120*, 2870–2879.

(12) Lai, Y. K.; Wong, K. Y. Electrochemistry of Oxo-Bridged Ruthenium Dimers with 4,4′-Dichloro- and 5,5′-Dichloro-2,2′-Bipyridine and Their Catalytic Properties towards Water Oxidation. *J. Electroanal. Chem.* **1995**, *380*, 193–200.

(13) Concepcion, J. J.; Jurss, J. W.; Templeton, J. L.; Meyer, T. J. Mediator-Assisted Water Oxidation by the Ruthenium "Blue Dimer" *cis*,*cis*-$[(bpy)_2(H_2O)RuORu(OH_2)(bpy)_2]^{4+}$. *Proc. Natl. Acad. Sci.* **2008**, *105*, 17632–17635.

(14) Notaro, A.; Gasser, G. Monomeric and Dimeric Coordinatively Saturated and Substitutionally Inert Ru(II) Polypyridyl Complexes as Anticancer Drug Candidates. *Chem. Soc. Rev.* **2017**, *46*, 7317–7337.

(15) Hess, J.; Keiser, J.; Gasser, G. Toward Organometallic Antischistosomal Drug Candidates. *Future Med. Chem.* **2015**, *7*, 821–830.

(16) Padhi, S. K.; Rai, S.; Akhter, S. S. Redox-Induced Structural Switching through Sporadic Pyridine-Bridged $Co^{II}Co^{II}$ Dimer and Electrocatalytic Proton Reduction. *Inorg. Chem.* **2020**, *59*, 7810–7821.

(17) Buvaylo, E. A.; Kokozay, V. N.; Vassilyeva, O. Y.; Skelton, B. W.; Ozarowski, A.; Titiš,

J.; Vranovičová, B.; Boča, R. Field-Assisted Slow Magnetic Relaxation in a Six-Coordinate Co(II)-Co(III) Complex with Large Negative Anisotropy. *Inorg. Chem.* **2017**, *56*, 6999–7009.

(18) Chandrasekhar, V.; Dey, A.; Mota, A. J.; Colacio, E. Slow Magnetic Relaxation in Co(III)-Co(II) Mixed-Valence Dinuclear Complexes with a $Co^{II}O_5X$ (X = Cl, Br, NO_3) Distorted-Octahedral Coordination Sphere. *Inorg. Chem.* **2013**, *52*, 4554–4561.

(19) Brazzolotto, D.; Cantú Reinhard, F. G.; Smith-Jones, J.; Retegan, M.; Amidani, L.; Faponle, A. S.; Ray, K.; Philouze, C.; de Visser, S. P.; Gennari, M.; Duboc, C. A High-Valent Non-Heme μ-Oxo Manganese(IV) Dimer Generated from a Thiolate-Bound Manganese(II) Complex and Dioxygen. *Angew. Chemie - Int. Ed.* **2017**, *56*, 8211–8215.

(20) Shova, S.; Vlad, A.; Cazacu, M.; Krzystek, J.; Ozarowski, A.; Malček, M.; Bucinsky, L.; Rapta, P.; Cano, J.; Telser, J.; Arion, V. B. Dinuclear Manganese(III) Complexes with Bioinspired Coordination and Variable Linkers Showing Weak Exchange Effects: A Synthetic, Structural, Spectroscopic and Computation Study. *Dalt. Trans.* **2019**, *48*, 5909–5922.

(21) Liu, J.; Krzystek, J.; Hill, S.; Barrios, L.; Aromí, G. Elucidating Magnetic Exchange and Anisotropy in Weakly Coupled Mn^{III} Dimers. *Inorg. Chem.* **2013**, *52*, 718–723.

(22) Reger, D. L.; Debreczeni, A.; Smith, M. D.; Jezierska, J.; Ozarowski, A. Copper(II) Carboxylate Dimers Prepared from Ligands Designed to Form a Robust π···π Stacking Synthon: Supramolecular Structures and Molecular Properties. *Inorg. Chem.* **2012**, *51*, 1068–1083.

(23) Reger, D. L.; Pascui, A. E.; Smith, M. D.; Jezierska, J.; Ozarowski, A. Halide and Hydroxide Linearly Bridged Bimetallic Copper(II) Complexes: Trends in Strong Antiferromagnetic Superexchange Interactions. *Inorg. Chem.* **2012**, *51*, 7966–7968.

(24) Triki, S.; Gómez-García, C. J.; Ruiz, E.; Sala-Pala, J. Asymmetric Azido-Copper(II) Bridges: Ferro- or Antiferromagnetic? Experimental and Theoretical Magneto-Structural Studies. *Inorg. Chem.* **2005**, *44*, 5501–5508.

(25) Reger, D. L.; Pascui, A. E.; Smith, M. D.; Jezierska, J.; Ozarowski, A. Syntheses, Structural, Magnetic, and Electron Paramagnetic Resonance Studies of Monobridged Cyanide and Azide Dinuclear Copper(II) Complexes: Antiferromagnetic Superexchange Interactions. *Inorg. Chem.* **2015**, *54*, 1487–1500.

(26) Nesterova, O. V.; Nesterov, D. S.; Jezierska, J.; Pombeiro, A. J. L.; Ozarowski, A. Copper(II) Complexes with Bulky N-Substituted Diethanolamines: High-Field Electron Paramagnetic Resonance, Magnetic, and Catalytic Studies in Oxidative Cyclohexane Amidation. *Inorg. Chem.* **2018**, *57*, 12384–12397.

(27) Capdevila, M.; Clegg, W.; González-Duarte, P.; Jarid, A.; Lledós, A. Hinge Distortion in Platinum(II) Dimers with a Pt_2S_2 Ring. An Ab Initio Molecular Orbital Study. *Inorg. Chem.* **1996**, *35*, 490–497.

(28) Gamelin, D. R.; Bominaar, E. L.; Kirk, M. L.; Wieghardt, K.; Solomon, E. I. Excited-State Contributions to Ground-State Properties of Mixed-Valence Dimers: Spectral and

Electronic-Structural Studies of $[Fe_2(OH)_3(Tmtacn)_2]^{2+}$ Related to the $[Fe_2S_2]^{+}$ Active Sites of Plant-Type Ferredoxins. *J. Am. Chem. Soc.* **1996**, *118*, 8085–8097.

(29) Crouse, B. R.; Meyer, J.; Johnson, M. K. Spectroscopic Evidence for a Reduced Fe_2S_2 Cluster with a S = 9/2 Ground State in Mutant Forms of Clostridium Pasteurianum 2Fe Ferredoxin. *J. Am. Chem. Soc.* **1995**, *117*, 9612–9613.

(30) Beardwood, P.; Gibson, J. F. $[Fe_2S_2(OAr)_4]^{2-}$: Iron-Sulphur Dimers with Terminal Phenolate Ligands. *J. Chem. Soc., Chem. Commun.* **1985**, *36*, 102–104.

(31) Shakurov, Gil'man S., Tarasov, V. F. High-Frequency Tunable EPR Spectroscopy of Cr^{3+} in Synthetic Forsterite. *Appl. Magn. Reson.* **2001**, *21*, 597–605.

(32) Gaister, A. V.; Konovalov, A. A.; Shakurov, G. S.; Subbotin, K. A.; Tarasov, V. F.; Zharikov, E. V. High-Frequency Two-Dimensional EPR Spectroscopy of Cr^{3+} and Ho^{3+} Dimers in Synthetic Forsterite. *Proc. SPIE* **2004**, *5478*, 46–54.

(33) Bershov, L. V.; Gaite, J.-M.; Hafner, S. S.; Rager, H. Electron Paramagnetic Resonance and ENDOR Studies of Cr^{3+}-Al^{3+} Pairs in Forsterite. *Phys. Chem. Miner.* **1983**, *9*, 95–101.

(34) Fraser, H. W. L.; Nichol, G. S.; Velmurugan, G.; Rajaraman, G.; Brechin, E. K. Magneto-Structural Correlations in a Family of Di-Alkoxo Bridged Chromium Dimers. *Dalt. Trans.* **2017**, *46*, 7159–7168.

(35) Scaringe, R. P.; Hodgson, D. J.; Hatfield, W. E. Exchange Coupling in Di-μ-Hydroxo-Bridged Chromium(III) Dimers. *Transit. Met. Chem.* **1981**, *6*, 340–344.

(36) Kremer, S. EPR Spectroscopic Study of S = 1, 2, and 3 Spin States of Tris(μ-Hydroxo)-Bridged Chromium(III) Dimers. *Inorg. Chem.* **1985**, *24*, 887–890.

(37) Ni, Z.-H.; Zhao, Y.-H.; Zheng, L.; Kou, H.-Z.; Cui, A.-L. A New Hydroxo-Bridged Chromium (III) Dimer $[Cr(Saltn)OH]_2 \cdot 4H_2O$: Synthesis, Crystal Structure and Magnetic Properties. *Chinese J. Chem.* **2005**, *23*, 786–790.

(38) Heinrichs, M. A.; Hodgson, D. J.; Michelsen, K.; Pedersen, E. Synthesis and Characterization of the Chromium(III) Dimer Bis(μ-hydroxo)bis[[*N*,*N*′-bis(2-pyridylmethyl)-l,2-ethanediamine]chromium(III)] Perchlorate, $[(bispicen)Cr(OH)]_2(C1O_4)_4 \cdot H2O$. *Inorg. Chem.* **1984**, *23*, 3174–3180.

(39) Scaringe, R. P.; Hatfield, W. E.; Hodgson, D. J. Magnetic and Structural Characterization of the Chromium(III) Dimer Sodium Di-μ-hydroxobis[bis(oxalato)chromate(III)] Hexahydrate, $Na_4[Cr(C_2O_4)_2OH]_2 \cdot 6H_2O$. *Inorganica Chim. Acta* **1977**, *22*, 175–183.

(40) J. Morsing, T.; Weihe, H.; Bendix, J. Probing Effective Hamiltonian Operators by Single-Crystal EPR: A Case Study Using Dinuclear Cr(III) Complexes. *Inorg. Chem.* **2016**, *55*, 1453–1460.

(41) McNeely, J.; Cage, B. DFT-BS Examination of Exchange Coupling in Chromium(III) Dimers Containing the $\mu_{1,2}$-Squarato Bridge. *Inorganica Chim. Acta* **2012**, *384*, 189–196.

(42) Tchougréeff, A. L.; Dronskowski, R. Effective Hamiltonian Crystal Field as Applied to Magnetic Exchange Parameters in μ-Oxo-Bridged Cr(III) Dimers. *J. Phys. Chem. A* **2013**,

117, 7980–7988.

(43) Morsing, T. J.; Sauer, S. P. A.; Weihe, H.; Bendix, J.; Døssing, A. Magnetic Interactions in Oxide-Bridged Dichromium(III) Complexes. Computational Determination of the Importance of Non-Bridging Ligands. *Inorganica Chim. Acta* **2013**, *396*, 72–77.

(44) Charlot, M. F.; Kahn, O.; Drillon, M. Correlation Structure-Magnetic Properties in $(Cr_2O_{10})^{14-}$ Dimeric Units: A Theoretical Approach. *Chem. Phys.* **1982**, *70*, 177–187.

(45) Semenaka, V. V.; Nesterova, O. V.; Kokozay, V. N.; Dyakonenko, V. V.; Zubatyuk, R. I.; Shishkin, O. V.; Boča, R.; Jezierska, J.; Ozarowski, A. Cr^{III}-Cr^{III} Interactions in Two Alkoxo-Bridged Heterometallic Zn_2Cr_2 Complexes Self-Assembled from Zinc Oxide, Reineckes Salt, and Diethanolamine. *Inorg. Chem.* **2010**, *49*, 5460–5471.

(46) Chakraborty, U.; Urban, F.; Mü, B.; Rebreyend, C.; De Bruin, B.; Van Velzen, N.; Harder, S.; Wolf, R. Accessing the $Cp^{Ar}Ni(I)$ Synthon: Reactions with N-Heterocyclic Carbenes, TEMPO, Sulfur, and Selenium. *Organometallics* **2016**, *35*, 1624–1631.

(47) Nomura, M. Organometallic Dithiolene Complexes of the Group 8–10 Metals: Reactivities, Structures and Electrochemical Behavior. *Dalt. Trans.* **2011**, *40*, 2112.

(48) Panda, C.; Menezes, P. W.; Walter, C.; Yao, S.; Miehlich, M. E.; Gutkin, V.; Meyer, K.; Driess, M. From a Molecular 2Fe-2Se Precursor to a Highly Efficient Iron Diselenide Electrocatalyst for Overall Water Splitting. *Angew. Chemie Int. Ed.* **2017**, *56*, 10506–10510.

(49) Azizpoor Fard, M.; Levchenko, T. I.; Cadogan, C.; Humenny, W. J.; Corrigan, J. F. Stable -$ESiMe_3$ Complexes of CuI and AgI (E=S, Se) with NHCs: Synthons in Ternary Nanocluster Assembly. *Chem. Eur. J.* **2016**, *22*, 4543–4550.

(50) Marsden, C. J.; Sheldrick, G. M. The Crystal and Molecular Structure of Bis{μ[(trifluoromethyl)selono]manganese tetracarbonyl}. *J. Organomet. Chem.* **1972**, *40*, 183–186.

(51) Song, L. C.; Cheng, H. W.; Hu, Q. M. Synthesis, Spectroscopic Characterization and Reactivities of Linear and Butterfly Chromium/Selenium Complexes Containing Substituted Cyclopentadienyl Ligands: Crystal Structures of $[\{\eta^5\text{-}MeC_5M_5H_4Cr(CO)_2\}_2Se]$ and $[\{\eta^5\text{-}EtO_2CC_5H_4Cr(CO)_2\}_2Se_2]$. *J. Organomet. Chem.* **2004**, *689*, 1849–1855.

(52) Chen, W.; Goh, L. Y.; Sinn, E. Chemistry of $[CpCr(CO)_3]_2$. An Insertion Mechanism for the Formation of $Cp_2Cr_2(CO)_5Se_2$ and $Cp_2Cr_2(CO)_4Se_2$ from $Cp_2Cr_2(CO)_4Se$. Carbonylation and Crystal Structure of $Cp_2Cr_2(CO)_4Se_2$. *Organometallics* **1988**, *7*, 2020–2026.

(53) Goh, L. Y.; Wei, C.; Sinn, E. Mono- and Di-Selenium Complexes of Chromium. Syntheses and Crystal Structures of $(\eta^5\text{-}C_5H_5)_2Cr_2(CO)_4Se$ and $(\eta^5\text{-}C_5H_5)_2Cr_2(CO)_4Se_2$. *J. Chem. Soc. Chem. Commun.* **1985**, 462–464.

(54) Thiele, G.; Santner, S.; Donsbach, C.; Assmann, M.; Müller, M.; Dehnen, S. Solvothermal and Ionothermal Syntheses and Structures of Amine- and/or (poly-)Chalcogenide Coordinated Metal Complexes. *Zeitschrift für Krist. - Cryst. Mater.* **2014**, *229*, 489–495.

(55) Gamage, E. H.; Greenfield, J. T.; Unger, C.; Kamali, S.; K. Clark, J.; Harmer, C. P.; Luo, L.; Wang, J.; Shatruk, M.; Kovnir, K. Tuning Fe–Se Tetrahedral Frameworks by a Combination of $[Fe(en)_3]^{2+}$ Cations and Cl^- Anions. *Inorg. Chem.* **2020**, *59*, 13353–13363.

(56) Toby, B. H.; Von Dreele, R. B. GSAS-II: The Genesis of a Modern Open-Source All Purpose Crystallography Software Package. *J. Appl. Crystallogr.* **2013**, *46*, 544–549.

(57) Sheldrick, G. M. Crystal Structure Refinement with SHELXL. *Acta Cryst. C* **2015**, *71*, 3-8.

(58) Hassan, A. K.; Pardi, L. A.; Krzystek, J.; Sienkiewicz, A.; Goy, P.; Rohrer, M.; Brunel, L. C. Ultrawide Band Multifrequency High-Field EMR Technique: A Methodology for Increasing Spectroscopic Information. *J. Magn. Reson.* **2000**, *142*, 300–312.

(59) Benelli, C.; Gatteschi, D. *Introduction to Molecular Magnetism: From Transition Metals to Lanthenides*; Wiley-VCH: Weinheim, Germany **2015**.

(60) Kallesøe, S.; Pedersen, E. Magnetic Properties of the Chromium(III) Dimer Delta(–)$_{546}$-Di-μ-hydroxo(*S*,*S*,*S*,*S*)-tetrakis(L-prolinato)dichromium(III) Tetrahydrate. *Acta Chem. Scand.* **1982**, *A36*, 859–860.

(61) Inoue, T.; Sugiyama, K.; Takeuchi, T.; Nakahanada, M.; Kaizaki, S.; Date, M. High Field Magnetization of Cr-Dimer Complexes. *J. Phys. Soc. Japan* **1992**, *61*, 4566–4571.

(62) Ciornea, V.; Mingalieva, L.; Costes, J. P.; Novitchi, G.; Filippova, I.; Galeev, R. T.; Shova, S.; Voronkova, V. K.; Gulea, A. Structural Determinations, Magnetic and EPR Studies of Complexes Involving the $Cr(OH)_2Cr$ Unit. *Inorganica Chim. Acta* **2008**, *361*, 1947–1957.

(63) Scaringe, R. P.; Singh, P.; Eckberg, R. P.; Hatfield, W. E.; Hodgson, D. J. Structural and Magnetic Characterization of Di-μ-hydroxo-bis[bis(1,10-phenanthroline(chromium(III)] Iodide Tetrahydrate. *Inorg. Chem.* **2002**, *14*, 1127–1133.

(64) Fischer, H. R.; Glerup, J.; Hodgson, D. J.; Pedersen, E. Structural and Magnetic Characterization of the Alkoxo-Bridged Chromium(III) Dimer Bis(μ-methoxo)bis[bis(2,4-pentanedionato)chromium(III)], $[(acac)_2Cr(OCH_3)]_2$. *Inorg. Chem.* **2002**, *21*, 3063–3066.

(65) Henning, J. C. M.; Damen, J. P. M. Exchange Interactions within Nearest-Neighbor Cr^{3+} Pairs in Chromium-Doped Spinel $ZnGa_2O_4$. *Phys. Rev. B* **1971**, *3*, 3852-3854.

(66) Kartsev, A.; Augustin, M.; Evans, R. F. L.; Novoselov, K. S.; Santos, E. J. G. Biquadratic Exchange Interactions in Two-Dimensional Magnets. *NPJ Comput. Mater.* **2020**, *6*, 150.

(67) Rodríguez-Fortea, A.; Alemany, P.; Alvarez, S.; Ruiz, E. Exchange Coupling in Halo-Bridged Dinuclear Cu(II) Compounds: A Density Functional Study. *Inorg. Chem.* **2002**, 41, 3769−3778.

(68) Onofrio, N.; Mouesca, J.-M. Analysis of the Singlet–Triplet Splitting Computed by the Density Functional Theory–Broken-Symmetry Method: Is It an Exchange Coupling Constant? *Inorg. Chem.* **2011**, *50*, 5577–5586.

(69) Malrieu, J. P.; Caballol, R.; J. Calzado, C.; de Graaf, C.; Guihéry, N. Magnetic Interactions in Molecules and Highly Correlated Materials: Physical Content, Analytical Derivation, and Rigorous Extraction of Magnetic Hamiltonians. *Chem. Rev.* **2013**, *114*, 429–492.

(70) Noodleman, L.; Case, D. A. Density-Functional Theory of Spin Polarization and Spin Coupling in Iron—Sulfur Clusters. *Adv. Inorg. Chem.* **1992**, *38*, 423–458.

(71) Noodleman, L.; Davidson, E. R. Ligand Spin Polarization and Antiferromagnetic Coupling in Transition Metal Dimers. *Chem. Phys.* **1986**, *109*, 131–143.

(72) Noodleman, L. Valence Bond Description of Antiferromagnetic Coupling in Transition Metal Dimers. *J. Chem. Phys.* **1998**, *74*, 5737–5743.

(73) Neese, F. The ORCA Program System. *Wiley Interdiscip. Rev. Comput. Mol. Sci.* **2012**, *2*, 73–78.

(74) Roos, B. O.; Taylor, P. R.; Sigbahn, P. E. M. A Complete Active Space SCF Method (CASSCF) Using a Density Matrix Formulated Super-CI Approach. *Chem. Phys.* **1980**, *48*, 157–173.

(75) Angeli, C.; Cimiraglia, R.; Evangelisti, S.; Leininger, T.; Malrieu, J.-P. Introduction of N-Electron Valence States for Multireference Perturbation Theory. *J. Chem. Phys.* **2001**, *114*, 10252.

(76) Neese, F. Calculation of the Zero-Field Splitting Tensor on the Basis of Hybrid Density Functional and Hartree-Fock Theory. *J. Chem. Phys.* **2007**, *127*, 164112.

TOC

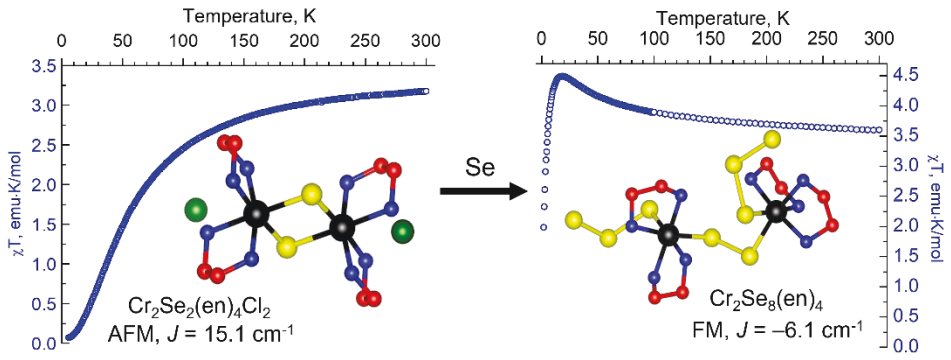

Dimer compounds $Cr_2Q_2(en)_4X_2$ (Q: S, Se; X: Br, Cl; *en*: ethylenediamine), with two monoatomic chalcogenide bridges and $Cr_2Se_8(en)_4$ with one diatomic Se bridge are reported. Monoatomic-bridged Cr_2Q_2 dimers show strong (Q = S) to moderate (Q = Se) antiferromagnetic Cr-Cr interactions according to high frequency EPR and magnetic studies. A replacement of monoatomic Se bridge with the diatomic one leads to change of Cr-Cr coupling to ferromagnetic.